JFM PAPERS

Modelling the relation between temperature and streamwise velocity fluctuations in compressible wall turbulence

Cheng Cheng[1,2] and **Lin Fu**[1,3]

[1]Department of Mechanical and Aerospace Engineering, The Hong Kong University of Science and Technology, Clear Water Bay, Kowloon, Hong Kong

[2]Institute for Advanced Study, The Hong Kong University of Science and Technology, Clear Water Bay, Kowloon, Hong Kong

[3]Department of Mathematics, The Hong Kong University of Science and Technology, Clear Water Bay, Kowloon, Hong Kong

Corresponding author: Lin Fu, linfu@ust.hk

In the present study, we investigate the relation between temperature (T') and streamwise velocity (u') fluctuations by assessing the state-of-the-art Reynolds analogy models. These analyses are conducted on three levels: in the statistical sense, in spectral space and via the distribution characteristics of temperature fluctuations. It is observed that the model proposed by Huang *et al.* (HSRA) (1995 *J. Fluid Mech.* **305**, 185–218), is the only model that works well for both channel flows and turbulent boundary layers in the statistical sense. In spectral space, the intensities of T' at small scales are discovered to be larger than the predictions of these models, whereas those at scales corresponding to the energy-containing eddies and the large-scale motions are approximately equal to and smaller than the predictions of the HSRA, respectively. The success of the HSRA arises from this combined effect. In compressible turbulent boundary layers, the relationship between the intensities of positive temperature and negative velocity fluctuations is found to be well described by a model proposed by Gaviglio (1987 *Intl J. Heat Mass Transfer*, **30**, 911–926), whereas that between negative temperature and positive velocity fluctuations is accurately depicted by the HSRA. The streamwise length scale, rather than the spanwise length scale, is found to be more suitable for characterising the scale characteristics of the $u' - T'$ relation in spectral space. Combining these observations and a newly proposed modified generalised Reynolds analogy (Cheng & Fu 2024 *J. Fluid Mech.* **999**, A20), models regarding the relations in spectral space for both compressible channel flows and turbulent boundary layers are developed, and a strategy for generating more reliable

temperature fluctuations as the inlet boundary condition for simulations of compressible boundary layers is also suggested.

1. Introduction

The Reynolds analogy model, which depicts the relationship between temperature and velocity fields, is a pacing item for predicting the thermal and aerodynamic force effects in high-speed wall-bounded turbulence. It is made up of two aspects: one is the relationship between the mean fields of these two fields, and another one is the counterpart for the fluctuating fields. Studies of the former have been constructed for nearly one hundred years since the work of Busemann (1931), and with the aid of direct numerical simulation (DNS) and large-eddy simulation (LES), substantial breakthroughs have been achieved in past decades (Busemann 1931; Crocco 1932; Morkovin 1962; Walz 1962; Duan & Martin 2011; Zhang *et al.* 2014; Song *et al.* 2023; Chen *et al.* 2024). However, for the latter, research is still underway. Numerous studies have focused on this subject in recent years (Chen *et al.* 2023*b*; Cogo *et al.* 2023; Cheng *et al.* 2024; Cheng & Fu 2024*c*; Gerolymos & Vallet 2024; Gibis *et al.* 2024). This is also the topic of the present study. We will comprehensively evaluate the existing relations between the two fluctuating fields and give some suggestions for their improvement. Hence, we will firstly recap the existing temperature–velocity fluctuating relationships developed over the last hundred years. Based on this, we will then introduce in detail the motivations of the present study.

1.1. *Crocco–Busemann relation and strong Reynolds analogy*

In the 1930s, Busemann (1931) and Crocco (1932) independently discovered the first temperature–velocity relationship for laminar flows, assuming that the fluid's Prandtl number (*Pr*) equals one. Later, van Driest (1951) expanded this relationship to turbulent boundary layers. Both studies highlight a strong analogy between the two fluctuating fields

$$H' = U_w u', \tag{1.1}$$

where H and u denote the total enthalpy and the streamwise velocity, respectively, and ξ' represents the fluctuating component of a variable ξ, which is the difference between the instantaneous value of ξ and its Reynolds-averaged statistic $\bar{\xi}$. The value of U_w is a constant for a boundary layer, which can be expressed as $U_w = -Pr\bar{q}_w/\bar{\tau}_w$ (q_w and τ_w denote the wall heat flux and the wall shear stress, respectively). Regarding an adiabatic boundary layer with $q_w = 0$, an exact relationship between the instantaneous u' and the temperature fluctuation T' can be deduced from (1.1), i.e.

$$T' = -\frac{\bar{u}}{C_p} u', \tag{1.2}$$

where C_p is the specific heat at constant pressure. Morkovin (1962) further proposed several statistical inferences, which are dubbed as the strong Reynolds analogy (SRA) and take the form of

$$C_{u'T'} = \frac{\overline{u'T'}}{\sqrt{\overline{u'^2}}\sqrt{\overline{T'^2}}} = -1, \tag{1.3}$$

$$Pr_t = \frac{\overline{\rho u' v'}}{\overline{\rho T' v'}} \frac{\partial \bar{T}}{\partial \bar{u}} = 1, \tag{1.4}$$

$$\frac{\sqrt{\overline{T'^2}}/\bar{T}}{(\gamma - 1)M^2\sqrt{\overline{u'^2}}/\bar{u}} = 1, \tag{1.5}$$

$$\frac{\sqrt{\overline{T'^2}}}{\bar{T}_w - \bar{T}_\delta} = 2\frac{\bar{u}}{\bar{u}_\delta}\frac{\sqrt{\overline{u'^2}}}{\bar{u}_\delta}, \tag{1.6}$$

where ρ, v, γ and M denote the density, the wall-normal velocity, the specific heat ratio and the local mean Mach number, respectively, and the subscripts 'w' and 'δ' denote the quantity evaluated at the wall and the boundary layer edge, respectively.

The Crocco–Busemann relation's assumption of $Pr = 1$ is highly idealised, given that $Pr \approx 0.7$ for air. In addition, the underling assumption of (1.2) is that the fluctuation of the total temperature (T_t') is negligible, which is contradicted by both experimental (Debieve *et al.* 1982; Gaviglio 1987) and DNS results (Guarini *et al.* 2000; Maeder *et al.* 2001; Duan *et al.* 2011). As a consequence, the SRA relations generally perform poorly. Only the relation (1.5) is satisfied by experiments and DNS of wall turbulence with adiabatic walls (Gaviglio 1987; Guarini *et al.* 2000). Several works attempted to extend the SRA to diabatic flows by considering the variation of mean total temperature within the boundary layer (Cebeci & Smith 1974; Gaviglio 1987). However, these extended versions still deviate from the real turbulence when heat transfer at the wall is non-negligible (Gaviglio 1987). We will not introduce them in detail here.

1.2. *Modified strong Reynolds analogy (MSRA)*

For the state-of-the-art relationships between these two fluctuating fields, the starting point is the phenomenological model reported by Gaviglio (1987). Gaviglio (1987) observed that, in a compressible boundary layer, the intensities of velocity and temperature fluctuations transported by large-scale eddies are proportional to the gradients of their mean quantities. Their corresponding ratios are positively related to the velocity length scale (ℓ_u) and the temperature length scale (ℓ_T), respectively. That is to say

$$a\sqrt{\overline{T'^2}}/\partial_y \bar{T} = \sqrt{\overline{u'^2}}/\partial_y \bar{u}, \tag{1.7}$$

where $a = \ell_u/\ell_T$, which is the ratio between the velocity and the temperature length scales; a is modelled as 1, 1.34 and the turbulent Prandtl number Pr_t in the model of Gaviglio (1987), Rubesin (1990) and Huang *et al.* (1995), respectively. Herein, we denote them as GSRA, RSRA and HSRA, respectively. A more commonly used form of (1.7) is

$$\frac{\sqrt{\overline{T'^2}}/\bar{T}}{(\gamma - 1)M^2\sqrt{\overline{u'^2}}/\bar{u}} = \frac{1}{a\left(1 - \partial \bar{T}_t/\partial \bar{T}\right)}, \tag{1.8}$$

where $T_t = T + u^2/(2C_p)$. Equation (1.7) can also be expressed in the instantaneous sense as follows:

$$aT'/\partial_y \bar{T} = u'/\partial_y \bar{u}. \tag{1.9}$$

Among the MSRA family, the statistical form of the HSRA, namely (1.7) or (1.8) with $a = Pr_t$, is reported to work best for wall turbulence with different wall thermal conditions (Huang *et al.* 1995; Pirozzoli *et al.* 2004; Duan & Martin 2011; Fu *et al.* 2021;

Huang *et al.* 2022). However, to the authors' knowledge, the instantaneous form in (1.9) has not been widely examined for its accuracy.

1.3. *Generalised Reynolds analogy model*

The generalised Reynolds analogy (GRA) proposed by Zhang *et al.* (2014) is a systematic model. They generalised the velocity–enthalpy relation by introducing a general recovery enthalpy H_g as follows:

$$\bar{H}_g - \bar{H}_w = U_w \bar{u}, \tag{1.10}$$

where $H_g = C_p T + r_g u^2/2$, and r_g is an extended form of the recovery factor. A residual temperature ϕ' is also introduced to build a weak analogy between the fluctuating velocity and temperature fields, namely

$$H_g' + C_p \phi' = U_w u'. \tag{1.11}$$

Combining (1.10) and (1.11), we can derive a governing differential equation for the mean quantities

$$\bar{T} - \frac{\bar{u}}{2} \left[\left. \frac{\partial \bar{T}}{\partial \bar{u}} \right|_w + \frac{1}{\overline{Pr_e}} \frac{\partial \bar{T}}{\partial \bar{u}} \right] = \bar{T}_w, \tag{1.12}$$

where $\overline{Pr_e}$ is called the effective Prandtl number by Zhang *et al.* (2014), whose definition is

$$\overline{Pr_e} \equiv \frac{\overline{Pr_t}}{1 + \varepsilon}, \quad \overline{Pr_t} \equiv \frac{\overline{(\rho v)'u'}}{\overline{(\rho v)'T'}} \frac{\partial \bar{T}}{\partial \bar{u}}, \quad \varepsilon = \frac{\overline{(\rho v)'\phi'}}{\overline{(\rho v)'T'}}, \tag{1.13}$$

where $\overline{Pr_t}$ is a new definition of the turbulent Prandtl number, and its value is only a little different from that of Pr_t (see (1.4)) in the outer layer of a boundary layer with a high Mach number (Zhang *et al.* 2014; Cheng & Fu 2023). For the fluctuating fields, their relation can also be deduced as

$$T' + \phi' = \frac{1}{\overline{Pr_e}} \frac{\partial \bar{T}}{\partial \bar{u}} u'. \tag{1.14}$$

Zhang *et al.* (2014) further assumed $\overline{Pr_e} = 1$, making (1.12) solvable. The final form of the deduced mean velocity–temperature relation is

$$\frac{\bar{T}}{\bar{T}_\delta} = \frac{\bar{T}_w}{\bar{T}_\delta} + \frac{\bar{T}_{rg} - \bar{T}_w}{\bar{T}_\delta} \frac{\bar{u}}{\bar{u}_\delta} + \frac{\bar{T}_\delta - \bar{T}_{rg}}{\bar{T}_\delta} \left(\frac{\bar{u}}{\bar{u}_\delta} \right)^2, \tag{1.15}$$

where $\bar{T}_{rg} = \bar{T}_\delta + r_g \bar{u}_\delta^2/(2C_p)$. This relation has been extensively verified by the DNS data (Zhang *et al.* 2014, 2018; Huang *et al.* 2022; Cogo *et al.* 2023). For the relation between the fluctuating fields, Zhang *et al.* (2014) modelled ϕ' as $(\overline{(\rho v)'\phi'}/\overline{(\rho v)'u'})u'$, and the HSRA can be restored with $a = \overline{Pr_t} \approx Pr_t$. Nevertheless, few studies have directly examined the accuracy of (1.14). Equation (1.14) suggests that a component of the temperature fluctuation (i.e. $T' + \phi'$) is coherent with the whole velocity fluctuation u'. If this scenario is unphysical, it implies that modelling ϕ' as $(\overline{(\rho v)'\phi'}/\overline{(\rho v)'u'})u'$ is only a makeshift. The statistical version of (1.14) is

$$(T' + \phi')_{rms} = \frac{1}{\overline{Pr_e}} \left| \frac{\partial \bar{T}}{\partial \bar{u}} \right| u'_{rms}, \tag{1.16}$$

where the subscript 'rms' denotes the root-mean-square value.

1.4. *Modified generalised Reynolds analogy model*

In a very recent work, the authors of the present study have modified the GRA by introducing a residual velocity χ' into the entire framework (hereafter, we denote this model as MGRA) (Cheng & Fu 2024c). We hypothesise that it is not u, but a new velocity u_e, named the local effective velocity, that constitutes the local effective recovery enthalpy (H_e), i.e. $H_e = C_p T + r_g u_e^2/2$. The local effective velocity can be decomposed into two components

$$u_e = u + \chi', \tag{1.17}$$

where χ' has a zero mean value but non-negligible fluctuation, and thus $\bar{u}_e = \bar{u}$. On the other hand, the generalised mean enthalpy–velocity relation is

$$\bar{H}_e - \bar{H}_w = U_w \bar{u}_e. \tag{1.18}$$

For the relationship between the fluctuating local effective enthalpy and velocity, the following formula can be introduced:

$$H_e' + C_p \phi' = U_w u_e', \tag{1.19}$$

where $H_e' = C_p T' + r_g \bar{u}_e u_e'$. Combining (1.18) and (1.19), the well-established $\bar{u} - \bar{T}$ relation (1.15) can also be deduced without assuming $\overline{Pr_e} = 1$. The reader can refer to our paper for a detailed derivation (Cheng & Fu 2024c). On the other hand, the $u' - T'$ relation is deduced to be

$$T' + \phi' = \frac{\partial \bar{T}}{\partial \bar{u}}(u' + \chi'). \tag{1.20}$$

It can be observed that, if we ignore the effect of χ', the present model can revert to the GRA. Equation (1.20) shows a distinct scenario compared with the GRA, that is, the duality relationship between u' and T' is more significantly broken, and only a component of u' (i.e. $u' + \chi'$) is linearly coherent with a component of T' (i.e. $T' + \phi'$). The new model is shown to be capable of eliminating the defects of the GRA, and demonstrated to be more accurate in depicting the relationship between u' and T'. The statistical version of (1.20) is

$$(T' + \phi')_{rms} = \left| \frac{\partial \bar{T}}{\partial \bar{u}} \right| (u' + \chi')_{rms}. \tag{1.21}$$

We have demonstrated that (1.21) is established in canonical compressible wall turbulence, with different geometries and wall thermal conditions. However, the instantaneous version, i.e. (1.20), has not yet been evaluated.

1.5. *Some remarks on the $u' - T'$ relations and motivations of present study*

As can be seen, the state-of-the-art $u' - T'$ relations can be classified into two types. One is those which sketch the relationship between the whole velocity and temperature fluctuations, including the SRA and the MSRA family. Another is the models which characterise the intrinsic duality relation between u' and T' tied by the mean fields. The latter includes the GRA and the MGRA. Note that the latter type of relation cannot be validated using the existing open-source statistical data of compressible flows, as they do not provide statistical information about ϕ' and χ'. Alternatively, some extra approaches should be deployed to dissect the instantaneous field, such as the spectral linear stochastic estimation (SLSE). This tool will be comprehensively introduced in § 3.

Model	Basic formula	Root-mean-square formula	Remark
SRA	$T' = -\bar{u}u'/C_p$	$(\sqrt{\overline{T'^2}}/\bar{T})/((\gamma-1)M^2\sqrt{\overline{u'^2}}/\bar{u}) = 1$	N/A
GSRA	$aT'/\partial_y\bar{T} = u'/\partial_y\bar{u}$	$a\sqrt{\overline{T'^2}}/\partial_y\bar{T} = \sqrt{\overline{u'^2}}/\partial_y\bar{u}$	$a = 1$
RSRA	$aT'/\partial_y\bar{T} = u'/\partial_y\bar{u}$	$a\sqrt{\overline{T'^2}}/\partial_y\bar{T} = \sqrt{\overline{u'^2}}/\partial_y\bar{u}$	$a = 1.34$
HSRA	$aT'/\partial_y\bar{T} = u'/\partial_y\bar{u}$	$a\sqrt{\overline{T'^2}}/\partial_y\bar{T} = \sqrt{\overline{u'^2}}/\partial_y\bar{u}$	$a = Pr_t$
GRA	$(T'+\phi')/\partial_y\bar{T} = u'/\partial_y\bar{u}$	$(T'+\phi')_{rms} = \left|\partial\bar{T}/\partial\bar{u}\right| u'_{rms}$	$\phi' = -T'_{nl}$
MGRA	$(T'+\phi')/\partial_y\bar{T} = (u'+\chi')/\partial_y\bar{u}$	$(T'+\phi')_{rms} = \left|\partial\bar{T}/\partial\bar{u}\right|(u'+\chi')_{rms}$	$\phi' = -T'_{nl}$, $\chi' = -u'_{nl}$

Table 1. The Reynolds analogy models for fluctuating fields involved in the present study. The definitions of T'_{nl} and u'_{nl} can be found in § 3.

The above-mentioned Reynolds analogy models for fluctuating fields are summarised in table 1.

Previous studies have extensively reported the validations of the statistical form of the SRA and the MSRA, namely, (1.5) and (1.8), in compressible channel flows (Huang *et al.* 1995; Brun *et al.* 2008) and turbulent boundary layers (Pirozzoli *et al.* 2004; Huang *et al.* 2022; Cogo *et al.* 2023). However, there are few assessments of the accuracy of the instantaneous versions of these relations, i.e. (1.2) and (1.9). Notwithstanding this, numerous studies have employed them to develop approaches to generate instantaneous flow fields of compressible wall-bounded turbulence. For example, Xu & Martin (2004) and Martin (2007) employed the SRA to obtain instantaneous temperature fluctuations through velocity fluctuations for constructing the inflow boundary condition of DNS of a compressible wall boundary layer with an adiabatic wall. Mo *et al.* (2023) also utilised the GSRA to achieve this. As a matter of fact, the establishment of a Reynolds analogy for instantaneous fields is quite strict. It is generally believed that u' and T' are two different kinds of physical quantities in compressible flows, and thus it is unrealistic for these relations to be true at every moment and spatial position. Nevertheless, it is still a seminal work to appraise the accuracy of the instantaneous versions of these relations under weaker conditions, for example, by examining the instantaneous distributions characteristics of T' according to them, to address the deficiencies of previous studies.

On the other hand, it can be seen that the relations between temperature field and streamwise velocity field described by all these models are all determined by the mean profiles of these two fields. Hence, a question arises: Does this kind of relation conform to the descriptions of various Reynolds analogy models at every scale in spectral space? Answering this question is another target of the present study. In summary, in the present work, we will systematically assess the existing Reynolds analogy models both in the statistical sense and in spectral space, including the two types of models summarised above. We believe that this work is revealing for the development of the related physical models and the simulation methodologies.

The remainder of this paper is organised as follows. In §§ 2 and 3, the DNS data and the analytical approaches are introduced, respectively. The relations between temperature field and streamwise velocity field in different levels are investigated via examining the state-of-the-art $u' - T'$ relations in § 4. In § 5, some discussions are given, such as the phase difference between u' and T', the relationship between the small-scale T' and u', the spectral models based on the foregoing results and a method for generating more reliable temperature fluctuations as the inlet boundary condition for the DNS/LES of compressible boundary layers. Concluding remarks are provided in § 6.

Case	M_b	Re_b	Re_τ	Re_τ^*	Δx^+	Δz^+	Δy_{min}^+	Δy_{max}^+	Tu_τ/h
Ma08Re17K	0.8	17 000	882	778	10.8	6.5	0.63	6.4	15.3
Ma15Re20K	1.5	20 020	1150	780	9.3	4.7	0.49	6.9	8.0
Ma30Re15K	3.0	15 000	1243	396	12.0	6.0	0.53	7.4	7.1

Table 2. Parameter settings of the compressible DNS database of channel flows. Here, Re_τ^* denotes the semi-local friction Reynolds number, Δx^+ and Δz^+ denote the streamwise and spanwise grid resolutions in viscous units, respectively, Δy_{min}^+ and Δy_{max}^+ denote the finest and coarsest resolution in the wall-normal direction, respectively and Tu_τ/h indicates the total eddy turnover time used to accumulate statistics.

Case	M_∞	Re_∞	$T_\infty(K)$	T_w/T_r	$L_x \times L_y \times L_z$	Re_τ	$t_s u_\infty/\delta_i$
M20T050	2.0	9081	220	0.5	$24.8\delta_i \times 8.1\delta_i \times 8.7\delta_i$	665–806	589.4
M20T100	2.0	26 631	220	1.0	$30.1\delta_i \times 8.2\delta_i \times 10.6\delta_i$	674–819	584.6
M80T050	8.0	422 782	51.8	0.5	$13.8\delta_i \times 6.8\delta_i \times 5.0\delta_i$	650–715	271.5
M80T100	8.0	1 186 116	51.8	1.0	$14.3\delta_i \times 7.0\delta_i \times 5.1\delta_i$	601–654	231.1

Table 3. The key parameters of DNS database of compressible turbulent boundary layers. Here, M_∞, Re_∞ and T_∞ represent the free-stream Mach number, Reynolds number and temperature, respectively; T_w/T_r denotes the ratio of isothermal wall temperature to recovery temperature; L_x, L_y and L_z denote the selected domain sizes along the streamwise, wall-normal and spanwise directions, respectively; δ_i and Re_τ represent the inlet boundary layer thickness and the friction Reynolds-number range of the selected domain, respectively; and $t_s u_\infty/\delta_i$ denotes the statistical sampling time period.

2. Direct numerical simulation database

The DNS database of compressible turbulent channel flows used here was generated in our previous studies (Cheng & Fu 2022, 2023). Cases with bulk Mach numbers $M_b = U_b/C_w = 0.8$, 1.5 and 3.0 (U_b is the bulk velocity, and C_w is the speed of sound at wall temperature) and bulk Reynolds numbers $Re_b = \rho_b U_b h/\mu_w = 17\,000$, 20 020 and 15 000 ($\rho_b$ denotes the bulk density, h the channel half-height and μ_w the dynamic viscosity at the wall) are selected. These cases were performed in a computational domain of $4\pi h \times 2\pi h \times 2h$ in the streamwise (x), spanwise (z), and wall-normal (y) directions, respectively, and are of the largest friction Reynolds number at the given M_b in our dataset. Details of the parameter settings of the database are tabulated in table 2. The details of the simulations and their validations are provided at length in Cheng & Fu (2022, 2023). We will not repeat them here for the sake of brevity.

The DNS database of supersonic and hypersonic turbulent boundary layers used here is built by Zhang *et al.* (2022), which is simulated by using an open-source solver STREAmS developed by Bernardini *et al.* (2021). For each case, a selected domain is adopted for analysing, and the parameters are provided in table 3. It can be observed that the Reynolds-number effects are negligible because the corresponding variation of Re_τ is not large. Under the circumstances, the two-dimensional (2-D) analysis introduced in § 3 can be applied. More details about the computational set-ups and the numerical methods regarding the DNS of this dataset can be found in Zhang *et al.* (2022).

Only the Reynolds-averaged and fluctuating statistics are utilised in the present study. Hereafter, we use the superscript '+' to represent normalisation with ρ_w, the friction velocity (denoted as u_τ, $u_\tau = \sqrt{\tau_w/\rho_w}$) and the viscous length scale (denoted as δ_v, $\delta_v = v_w/u_\tau$, $v_w = \mu_w/\rho_w$). We also use the superscript '*' to represent normalisation with the semi-local units, i.e. $u_\tau^* = \sqrt{\tau_w/\overline{\rho}}$ and $\delta_v^* = \overline{v(y)}/u_\tau^*$. Additionally, for turbulent

boundary layers, δ denotes the mean boundary layer thickness of the selected region for each case tabulated in table 3. To avoid lengthy descriptions, in § 4, we only use a turbulent channel flow case Ma15Re20K and two cases of boundary layers M20T050 and M20T100 to display the general results . Other cases listed in table 2 and table 3 will be used in § 5 to discuss the modelling approach.

3. Diagnostic tool and methodology

As we mentioned in the introduction, the original versions of the $u' - T'$ relations indicated by the GRA and the MGRA cannot be examined by using the open-source data, which only contain the mean and fluctuating statistics of a compressible flow due to the existence of the residual temperature and velocity fluctuations, i.e. ϕ' and χ'. Taking (1.14) as an example, an additional approach should be resorted to extracting the component of T' which is linearly coherent with u' at a given wall-normal locus (denoted as T_l'). Only by comparing the intensities of T_l' with $(\partial \bar{T}/\partial \bar{u})u'$, can we validate (1.14). Hence, we adopt the SLSE herein.

The SLSE is a data-driven decomposition method for investigating the multiphysics couplings in both the incompressible and compressible wall-bounded turbulence (for example, Baars *et al.* 2017, Wang *et al.* 2021, Cheng & Fu 2023 and Ying *et al.* 2024, to name a few). This method quantifies the linear correlation between two flow variables and enables the reconstruction of a target physical quantity's instantaneous signal using another variable as the input. Owing to the inherent linearity of the SLSE approach, the estimated signal maintains a strictly linear relationship with the input signal. It takes the form of

$$T_l'(y) = F_{x,z}^{-1}\left\{H_{Tu}(\lambda_x, \lambda_z; y) \, F_{x,z}[u'(y)]\right\}, \tag{3.1}$$

where $F_{x,z}$ and $F_{x,z}^{-1}$ denote the 2-D fast Fourier transform (FFT) and the inverse 2-D FFT in the streamwise and the spanwise directions, respectively. Here, H_{Tu} is the transfer kernel, which gauges the correlation between $\hat{T}'(y)$ and $\hat{u}'(y)$ at streamwise length scale λ_x and spanwise length scale λ_z, and can be calculated as

$$H_{Tu}(\lambda_x, \lambda_z; y) = \frac{\langle \hat{T}'(\lambda_x, \lambda_z; y) \, \check{\hat{u}}'(\lambda_x, \lambda_z; y)\rangle}{\langle \hat{u}'(\lambda_x, \lambda_z; y) \, \check{\hat{u}}'(\lambda_x, \lambda_z; y)\rangle}, \tag{3.2}$$

where $\langle \cdot \rangle$ denotes the ensemble averaging, $\hat{u}'$ and $\hat{T}'$ are the Fourier coefficients of u' and T', respectively, and $\check{\hat{u}}'$ represents the complex conjugate of $\hat{u}'$. In this regard, the uncorrelated component can be calculated as $T_{nl}' = T' - T_l'$. Similarly, we can also extract the component of u' that holds a linear relationship with T', that is

$$u_l'(y) = F_{x,z}^{-1}\left\{H_{uT}(\lambda_x, \lambda_z; y) \, F_{x,z}[T'(y)]\right\}, \tag{3.3}$$

where the kernel function H_{uT} can be constructed by analogy. We will not show it here for the sake of brevity. The uncorrelated component can be calculated as $u_{nl}' = u' - u_l'$. Additionally, to measure the overall coherence of T' and u' at a given length scale, a 1-D linear coherence spectrum (LCS) can also be introduced. Taking the streamwise length scale λ_x as an example, the LCS can be expressed as

$$\gamma^2\,(\lambda_x;\,y) = \frac{|\langle \hat{T}'\,(\lambda_x;\,y)\,\breve{\hat{u}}'\,(\lambda_x;\,y)\rangle|^2}{\langle |\hat{T}'\,(\lambda_x;\,y)\,|^2\rangle\langle |\hat{u}'\,(\lambda_x;\,y)\,|^2\rangle}, \tag{3.4}$$

where $|\cdot|$ is the modulus. Here, γ^2 evaluates the square of the scale-specific correlation between $T'(y)$ and $u'(y)$ with $0 \leqslant \gamma^2 \leqslant 1$. To be specific, $\gamma^2 = 1$ suggests a perfectly linear correlation between the velocity and temperature signals at a given λ_x, whereas $\gamma^2 = 0$ implies a purely uncorrelated relationship. The physical implication of γ^2 given here is an extension of that of the one-point correlation function in physical space, the reader can refer to Bendat & Piersol (2011), Baars *et al.* (2016) and Cheng & Fu (2023) for more details. In Cheng & Fu (2023), we employed γ^2 to shed light on the physical mechanisms of the $u' - T'$ coupling at a given wall-normal position in supersonic channel flows. We observed that γ^2 is of large values at the scales corresponding to the energy-containing motions populating this wall-normal locus. The spanwise version $\gamma^2(\lambda_z;\,y)$ can be defined similarly.

As per the linear nature of the SLSE, it is not difficult to observe that, if the GRA is correct, $T' + \phi'$ in (1.14) should be T'_l in (3.1), because it is just the component of T' that shares a linear relationship with u'. Similarly, if the MGRA is sufficiently accurate, $T' + \phi'$ and $u' + \chi'$ in (1.20) should be T'_l and u'_l, respectively, and thus $-\phi'$ and $-\chi'$ ought to be T'_{nl} and u'_{nl}, respectively. The parameters T'_{nl} and u'_{nl} are the small-scale components of T' and u', respectively, which are free from the influences of the mean fields (Cheng & Fu 2024*c*). Hence, we can appraise these two models directly with the SLSE serving as an effective tool.

To further inspect the relation between u' and T' in scale space, a 1-D ratio function can be defined, namely

$$RS_{uT}\,(\lambda_x;\,y) = \sqrt{\frac{\langle |\hat{T}'\,(\lambda_x;\,y)\,|^2\rangle}{\langle |\hat{u}'\,(\lambda_x;\,y)\,|^2\rangle}}. \tag{3.5}$$

The parameter $RS_{uT}(\lambda_x;\,y)$ inherently evaluates the 'energy ratio' between T' and u' at a wavelength λ_x. Similar definition and physical explanation are also given in Gupta *et al.* (2021) and Cheng & Fu (2023). In addition, the function associated with T'_l and u'_l can also be defined and denoted as $RS_{u_l T_l}$. It is noted that these functions can also be defined as functions of the spanwise length scale λ_z in a similar way.

The values of these ratio functions at a selected wavelength can be compared with those indicated by the SRA, the MSRA, the GRA and the MGRA, i.e.

$$f_0(y) = \left| \frac{\bar{u}}{C_p} \right|, \tag{3.6}$$

$$f_1(y) = \left| \frac{1}{a} \frac{\partial \bar{T}}{\partial \bar{u}} \right|, \tag{3.7}$$

$$f_2(y) = \left| \frac{\partial \bar{T}}{\partial \bar{u}} \right|. \tag{3.8}$$

Note that, the magnitude of $a = Pr_t$ in (3.7) for the HSRA is computed from the DNS data, unless otherwise specified.

4. Results

4.1. *Relation between temperature and streamwise velocity fluctuations*

The relation between temperature and streamwise velocity fluctuations can be dissected at three levels. The first is the overall relation, namely, the ratio between the statistical moments of these two fluctuating fields. This level of relation is associated with the descriptions of the statistical forms of the MSRA (cf. (1.7)), the GRA (cf. (1.16)) and the MGRA (cf. (1.21)). The second level is the relation in spectral space, namely, their intensities at each length scale. Since $u' - T'$ coupling is documented to be linked with the multi-scale eddies (Cheng & Fu 2023, 2024*b*), and thus this level of relation can also be hypothesised to be scale-dependent and Reynolds-number dependent. To the best knowledge of the authors, it has not been clarified before. The third level of relation is in the realm of instantaneous fields, namely, to what extent do the distribution characteristics of T' follow the delineation of the existing Reynolds analogy models. In this section, we will elaborate on these three aspects in return.

4.1.1. *Overall relation between temperature and streamwise velocity fluctuations*

Let us examine the MSRA family first. Although this kind of work has been reported by previous studies extensively, we still include them here for the completeness of the present study. To facilitate comparison, a ratio function is defined as $r_1 = ((1/a)|(\partial \bar{T}/\partial \bar{u})|u'_{rms})/T'_{rms}$.

Figures 1(*a*), 1(*c*) and 1(*e*) show the variations of r_1 for different Reynolds analogy models in a turbulent channel flow and two boundary layers with varying wall thermal conditions. For the channel flow, it can be found that the HSRA works excellently in the near-wall region, and gradually deteriorates when $y/h > 0.3$. For the GSRA and the RSRA, the values of r_1 deviate significantly from unity throughout the entire channel. Apparently, for this kind of flow, the HSRA is the most accurate model in the statistical sense. For the turbulent boundary layer with an adiabatic wall, the scenario is distinct. The values of r_1 associated with the HSRA and the GSRA are slightly larger and smaller than unity, respectively, while that of the RSRA deviates from it significantly. However, when the flow over a cold wall is taken into consideration, the performance of the HSRA is the best, whereas those of the RSRA and the GSRA are drastically worse. In summary, the accuracy of the GSRA is case-dependent and relies on the wall temperature and the geometry of the flow. By contrast, the HSRA is the most accurate, and the RSRA is the least accurate.

Next, we verify the predictions of the GRA and the MGRA. To this end, we also define two ratio functions $r_2 = (|\partial \bar{T}/\partial \bar{u}|u'_{rms})/T'_{l,rms}$ and $r_3 = (|\partial \bar{T}/\partial \bar{u}|u'_{l,rms})/T'_{l,rms}$. Figures 1(*b*), 1(*d*) and 1(*f*) display their distributions for all cases mentioned above. Apparently, the performance of the MGRA is superior to that of the GRA for all cases, except within the near-wall region of a turbulent boundary layer with a diabatic wall. It highlights the fact that the MGRA provides a more accurate description of the intrinsic duality relation between u' and T' tied by the mean fields (for more physical analyses, one can refer to Cheng & Fu 2024*c*). Hence, in the following analyses, we mainly concentrate on the MGRA rather than the GRA.

To gain more insights into the relation between u' and T', in figure 2, we show the variations of $\overline{u'^2_{nl}}/\overline{u'^2}$ and $\overline{T'^2_{nl}}/\overline{T'^2}$ for these two types of flows. As can be seen, for a turbulent boundary layer with an adiabatic wall, the majority of the energy of u' is contained in u'_{nl} in the near-wall region, i.e. the component of u' which is not linearly coherent with T'. The ratio $\overline{u'^2_{nl}}/\overline{u'^2}$ decreases with the increase of the wall-normal height
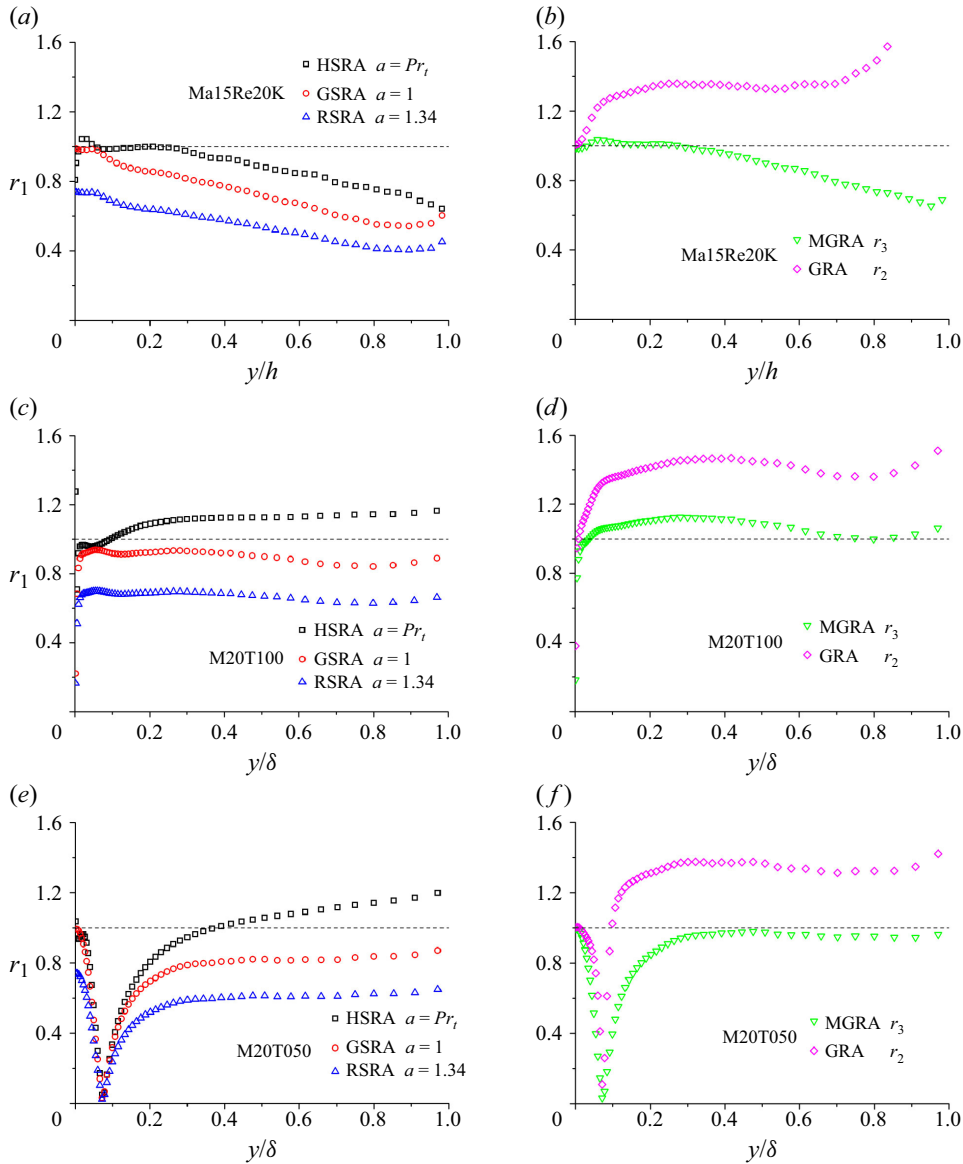
Figure 1. (a,c,e) Variations of ratio function r_1 for the MSRA models in (a) a turbulent channel flow Ma15Re20K, (c) a boundary layer with an adiabatic wall M20T100 and (e) a boundary layer with a cold wall M20T050; (b,d,f) variations of ratio functions r_2 and r_3 for the GRA and the MGRA in (b) a turbulent channel flow Ma15Re20K, (d) a boundary layer with an adiabatic wall M20T100 and (f) a boundary layer with a cold wall M20T050.

and maintains a nearly constant value in the outer region. For the case with a diabatic wall, most of the energy of u' is contained in u'_{nl} in the proximity of the location of the peak of $\bar{T}$. Similar observations can be made between T'_{nl} and T'. For a channel flow, a greater proportion of the fluctuation intensities of u' and T' are retained in u'_{nl} and T'_{nl} with the increase of the wall-normal height, respectively. All these information suggests that $u' - T'$ coupling is heavily influenced by the wall thermal boundary conditions and the geometries of the flows.
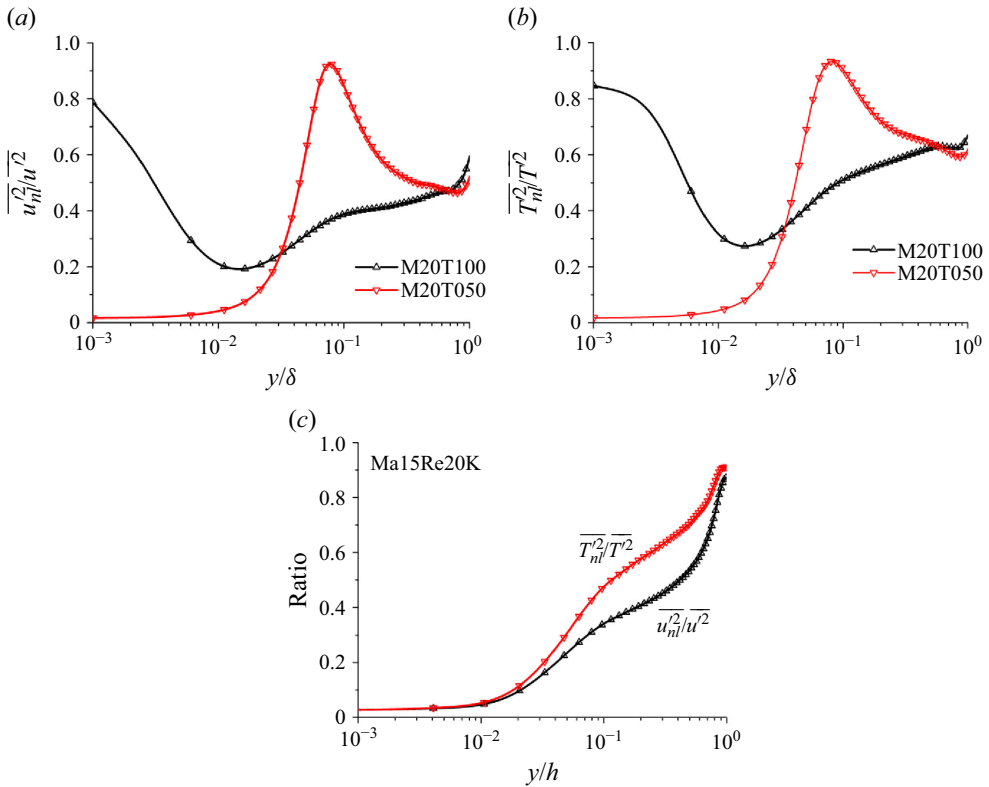
Figure 2. (*a,b*) Variations of (*a*) $\overline{u_{nl}'^2}/\overline{u'^2}$ and (*b*) $\overline{T_{nl}'^2}/\overline{T'^2}$ for turbulent boundary layers; (*c*) the counterparts for a channel flow case Ma15Re20K.

4.1.2. *Relation between temperature and streamwise velocity fluctuations in spectral space*

In the upper subsection, we show the results of the so-called first-level relation, i.e. the overall relation in the statistical sense. A natural question arises: Is there the same relationship at each scale? It would certainly be interesting to explore this aspect. To measure the relative intensity at each scale with respect to the predictions of the above-mentioned models, the following error functions are defined:

$$\epsilon_T = \frac{RS_{uT} - f_1}{f_1} \times 100\,\%, \tag{4.1}$$

$$\epsilon_{T_l} = \frac{RS_{u_l T_l} - f_2}{f_2} \times 100\,\%. \tag{4.2}$$

Here, ϵ_T and ϵ_{T_l} gauge the relative intensities of T' and T_l' with respect to u' and u_l' in spectral space, and are tailored for the MSRA family and the MGRA, respectively. If ϵ_T (ϵ_{T_l}) is larger than 0, it suggests that T' (T_l') responds stronger than the overall intensity predicted by (1.7) ((1.21)) at a given length scale, and *vice versa*. It is to be noted that, although the HSRA is demonstrated to be the most accurate one among the MSRA family in the statistical sense, we still compare all these models in spectral space herein, because other members, such as the SRA and the GSRA, are still frequently adopted or modified for generating instantaneous temperature field because of their conciseness (Xu & Martin 2004; Martin 2007; Mo *et al.* 2023). We will report the results of the MSRA family and the MGRA in turn.
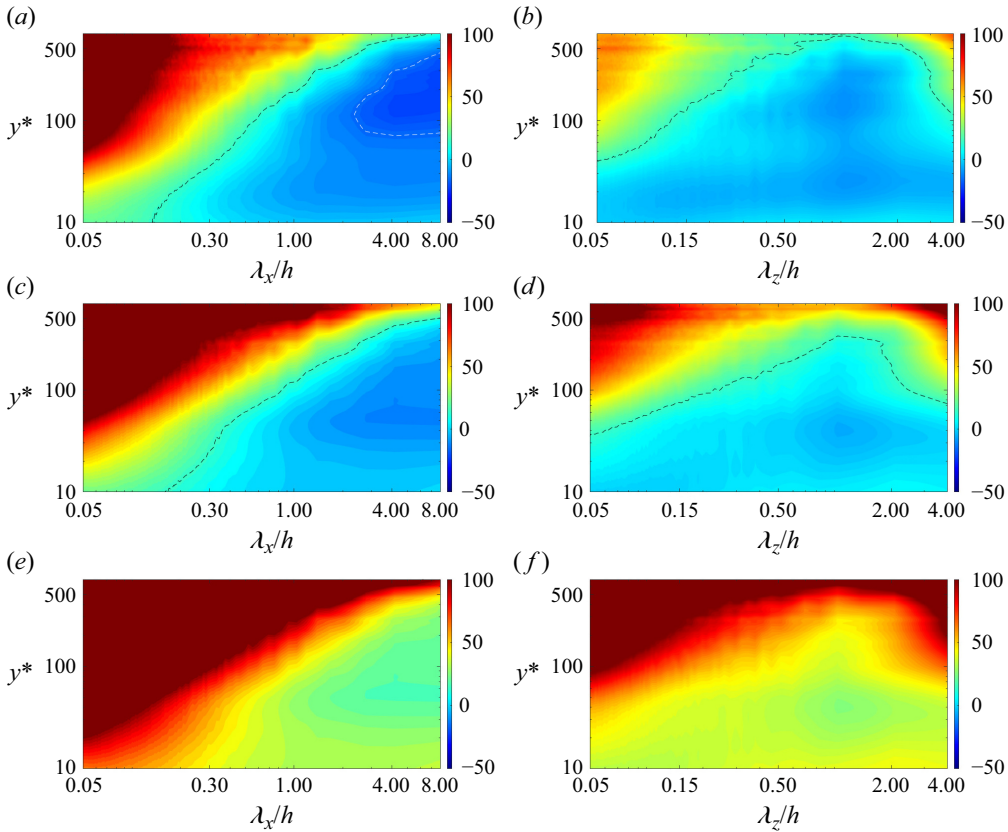
Figure 3. Distributions of the error function ϵ_T with respect to (a,c,e) streamwise and (b,d,f) spanwise length scales, which are related to : (a,b) HSRA, (c,d) GSRA, (e,f) RSRA. A channel case Ma15Re20K is taken into consideration. The value in each panel is expressed as a percentage count. The black and white dashed lines in panels are 15 % and −15 % isolines, respectively.

Let us look at the results of the channel flow Ma15Re20K first. Figure 3 shows distributions of the error function ϵ_T with respect to the (a,c,e) streamwise and (b,d,f) spanwise length scales covering the whole channel, respectively. The results of the (a,b) HSRA, the (c,d) GSRA, and the (e,f) RSRA are displayed for comparison. It bears emphasising that the wall-normal distribution of $\bar{T}$ is of no extreme point for this kind of flow. For the HSRA, it can be observed that the value of ϵ_T is nearly zero for $y^* < 20$ at all scales, for both the streamwise and spanwise scales. It implies that T' and u' at each scale are of fluctuation intensities predicted by the HSRA below the buffer layer. However, for $y^* > 20$, the scales with small λ_x and λ_z are of significantly stronger temperature fluctuation intensities than the prediction, whereas for large scales, their behaviours still follow the HSRA's prediction. This is the underlying reason why the magnitude of r_1 related to the HSRA is remarkably smaller than unity in the outer region, see figure 1(a). Only the temperature fluctuations at scales corresponding to the energy-containing motions behave according to the intensity given by the HSRA, whereas those at small scales are stronger than the model prediction. In §5.3, we will discuss the scale boundaries of these two regimes. For the other two models, the spectral ranges where $\epsilon_T > 0$ are wider than those of the HSRA. Even the scales with large and moderate λ_z are of stronger temperature fluctuation intensities than their predictions in the outer region,
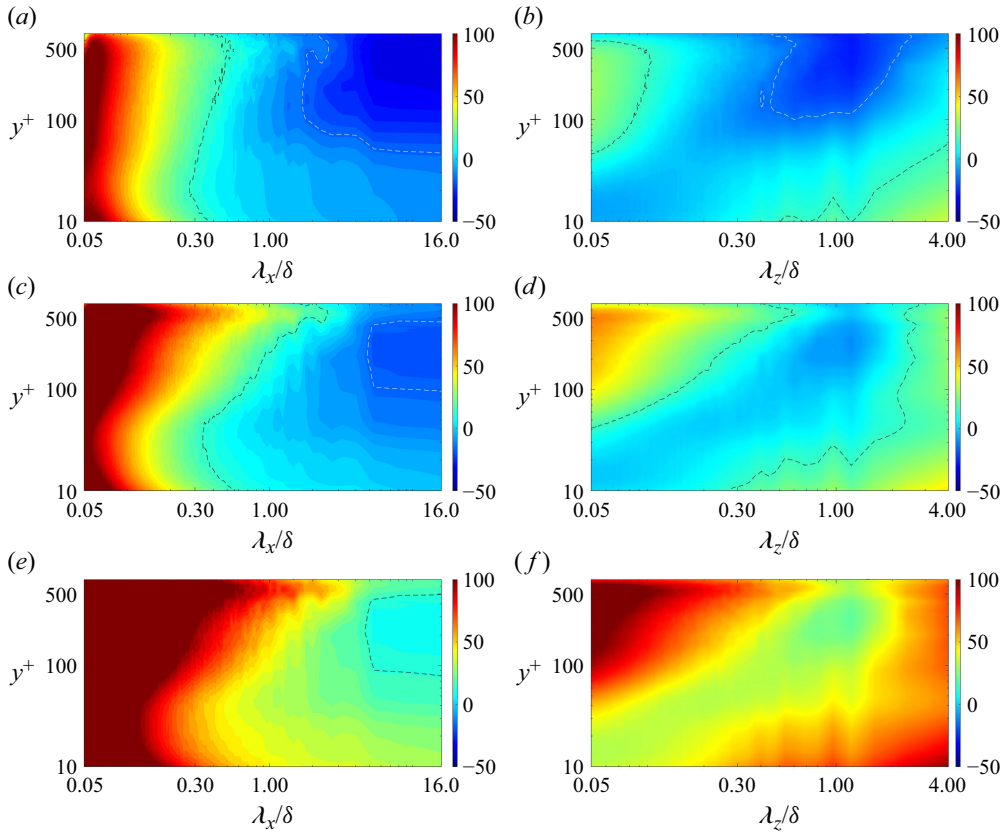
Figure 4. Distributions of the error function ϵ_T with respect to (a,c,e) streamwise and (b,d,f) spanwise length scales, which are related to: (a,b) HSRA, (c,d) GSRA, (e,f) RSRA. A turbulent boundary layer case with an adiabatic wall M20T100 is taken into consideration. The value in each panel is expressed as a percentage count. The black and white dashed lines in panels are 15 % and −15 % isolines, respectively.

see figure 3(b,d,f). It highlights the limitations of the GSRA and the RSRA for the channel flow.

The counterparts for the case Ma20T100, namely, a turbulent boundary layer with an adiabatic wall, are shown in figure 4. For this case, the wall-normal distribution $\bar{T}$ is also of no extreme point. Interestingly, for the HSRA, its performance is not entirely similar to that observed in the turbulent channel flow in spectral space. At an arbitrary wall-normal position, even below the buffer layer, value of ϵ_T varies gradually with increasing λ_x. To be specific, the temperature fluctuation intensities at small λ_x are stronger than the prediction of the model. As the increase of λ_x, the velocity and temperature intensities at the corresponding scales gradually tend to follow the prediction. However, in the range of $y^+ > 100$, for wavelengths with $\lambda_x > 2\delta$ and $\lambda_z \approx 1\delta$, values of ϵ_T can be found to be smaller than zero. In other words, the first-level relation successfully described by the HSRA is a comprehensive outcome of this multi-scale effect. For the GSRA, it can be seen that the small-scale region with large errors in spectral space is wider than that of the HSRA, while for wavelengths within $2\delta < \lambda_x < 4\delta$, its accuracy is higher. This explains why the magnitudes of r_1 for the HSRA and the GSRA are larger and smaller than unity, respectively (see figure 1c). For the RSRA, the relations between velocity and temperature fluctuation intensities at almost all scales are poorly predicted. As a sanity check, the
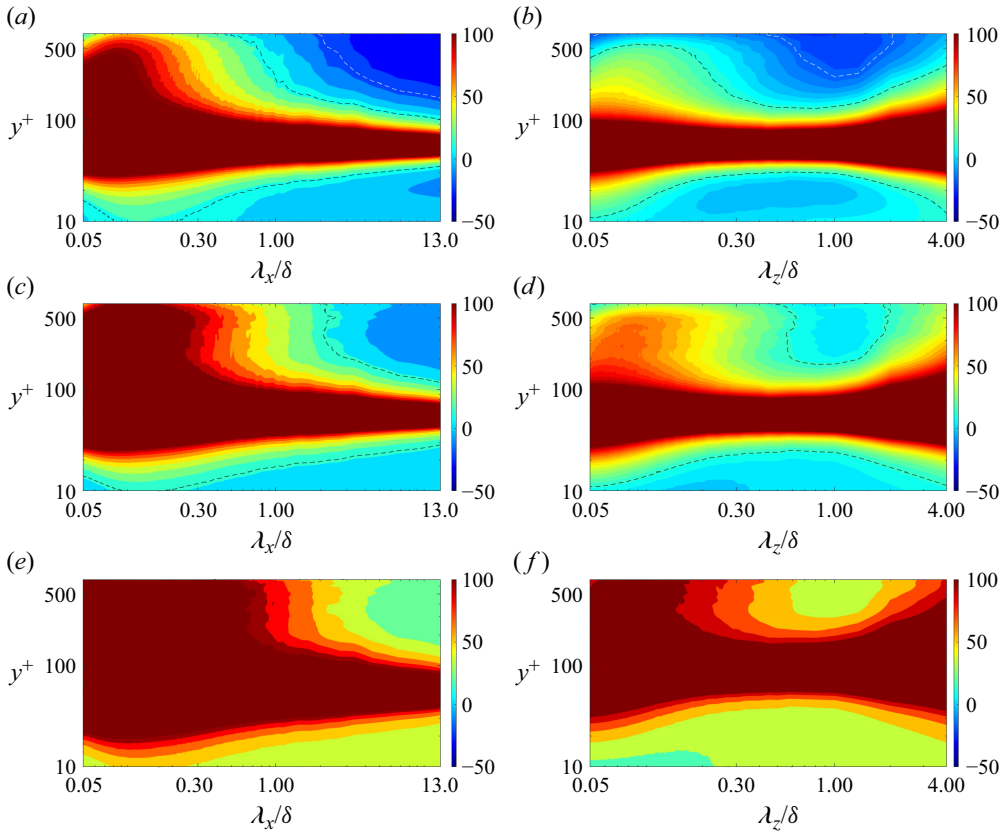
1017 A34-14

Figure 5. Distributions of the error function ϵ_T with respect to (a,c,e) streamwise and (b,d,f) spanwise length scales, which are related to: (a,b) HSRA, (c,d) GSRA, (e,f) RSRA. A turbulent boundary layer case with a cold wall M20T050 is taken into consideration. The value in each panel is expressed as a percentage count. The black and white dashed lines in panels are 15 % and -15 % isolines, respectively.

results associated with the SRA for the case with an adiabatic wall are supplemented in Appendix A.

Figure 5 exhibits the counterparts for the case Ma20T050, a turbulent boundary layer with a diabatic wall. The local maximum of $\bar{T}$ is located at $y^+ \approx 55$, and thus the distribution of Pr_t is singular near this wall-normal location. Apparently, all models belonging to the MSRA family fail to give a precise description of the $u' - T'$ relation in the wall-normal region adjacent to the local maximum of $\bar{T}$ for all scales. The further away from the extreme point of $\bar{T}$, the more accurately the HSRA predicts the relation at intermediate-scale range. However, this model still performs poorly for small scales in the outer region. For other two models, their performance is visibly worse than that of the HSRA, even away from the location of the extreme point of $\bar{T}$.

All in all, for flows with different geometries and wall thermal conditions, the most accurate model in the MSRA family is the HSRA. It can describe well the $u' - T'$ relations at all scales only below the buffer layer of a compressible channel flow. Besides, for the small scales in turbulent boundary layers, the temperature fluctuation intensities of them are larger than the predictions given by all models of the MSRA family. For the large scales, their temperature intensities are lower than that given by the HSRA, but better predicted by the GSRA. Only the fluctuation intensities at the moderate scales, i.e. those
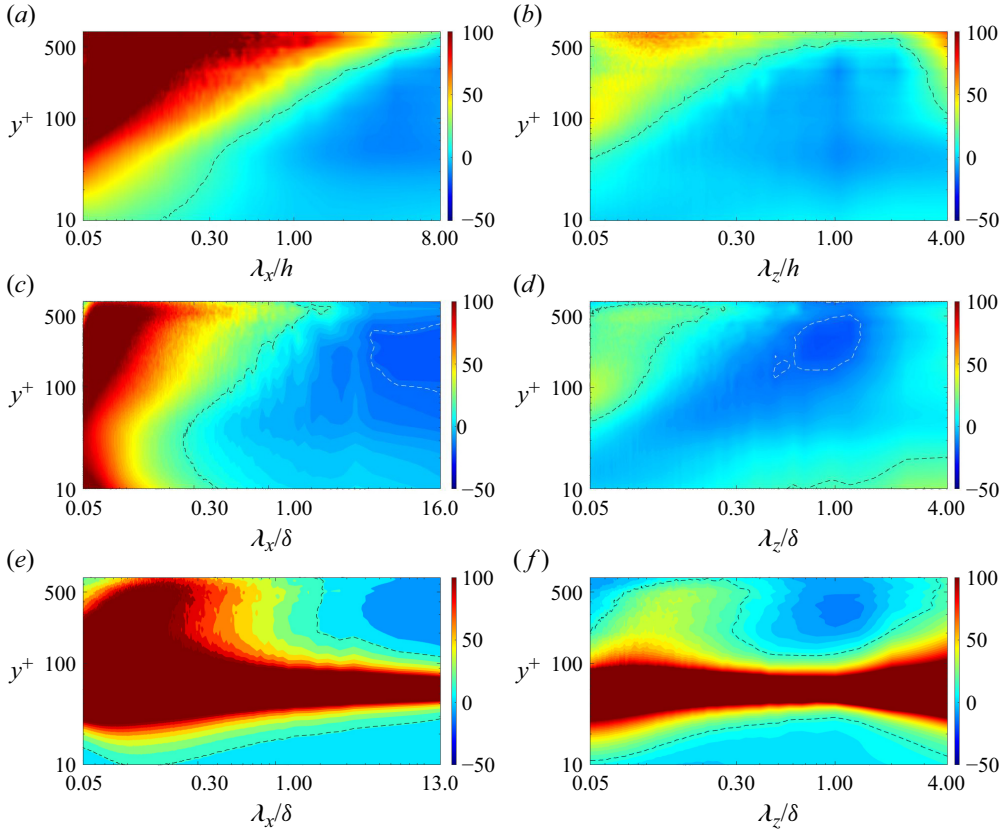
Figure 6. Distributions of the error function ϵ_{Tl} with respect to (a,c,e) streamwise and (b,d,f) spanwise length scales. The cases are: (a,b) a turbulent channel flow Ma15Re20K, (c,d) a boundary layer with an adiabatic wall M20T100, (e,f) a boundary layer with a cold wall M20T050. The MGRA is taken into consideration. The value in each panel is expressed as a percentage count. The black and white dashed lines in panels are 15 % and −15 % isolines, respectively.

corresponding to the energy-containing eddies, follow the prediction of the HSRA. The success of the HSRA arises from this combined effect. None of these models can depict the $u' - T'$ relation in the region where the extreme point of $\bar{T}$ profile appears.

For the second type of the $u' - T'$ relation summarised in the introduction, we can also resort to the distributions of ϵ_{Tl} for all cases to shed light on the relation between the u'_l and T'_l, which are exhibited in figure 6. Note that, u'_l and T'_l are energetic at moderate and large scales, not small scale (Cheng & Fu 2024c). Compared with the distributions of ϵ_T shown above, it is not difficult to observe that the diagrams resemble those of the GSRA at each case. A notable aspect is that for the case M20T100, the values of ϵ_{Tl} at large scales with $\lambda_x > 4\delta$ in the outer region are close to f_2, which are not adequately predicted by the HSRA, but well predicted by the GSRA. This is the reason that the MGRA outperforms the HSRA in the intermittent layer of a boundary layer, see figure 1.

As a final note, the present analyses highlight the multi-scale behaviours of temperature fluctuations. The intensities of T' at small scales are higher than the predictions of the models. This is expected, as small-scale eddies are intermittent and accompanied by extreme events (Frisch & Donnelly 1996). On the contrary, the fluctuations at large scales

are typically low in amplitude. Only the fluctuations at moderate scales, which are dictated by the mean fields, can be described by the Reynolds analogy models (Cheng & Fu 2024*c*).

4.1.3. *Distribution characteristics of temperature fluctuations according to the Reynolds analogy models*

At last, let us turn to the relation regarding distribution characteristics of T'. To facilitate the description, we denote T_s', T_h', T_g', T_r' and T_{mg}' as $-(\bar{u}/C_p)u'$, $(1/Pr_t)(\partial \bar{T}/\partial \bar{u})u'$, $(\partial \bar{T}/\partial \bar{u})u'$, $(1/1.34)(\partial \bar{T}/\partial \bar{u})u'$ and $(\partial \bar{T}/\partial \bar{u})u_l'$, respectively. Their instantaneous properties can be compared with those of the instantaneous signals of T' and T_l' obtained from DNS accordingly.

Figures 7(*a*), 7(*c*) and 7(*e*) show the probability density functions (p.d.f.s) of T_h', T_g' and T_r' at (*a*) $y^* = 10$, (*c*) $y = 0.2h$, (*e*) $y = 0.5h$ for Ma15Re20K, which correspond to the near-wall region, the logarithmic region and the outer region, respectively. The p.d.f. of T' at each wall-normal locus is also added for comparison. One can observe that, in the near-wall region, the p.d.f.s of T_h', T_g' and T_r' are close to that of T', indicating the success of the MSRA family in this region. Moreover, the p.d.f.s of T_h' and T_g' nearly collapse with each other due to $Pr_t \approx 1$ in the vicinity of the wall for a channel flow. On the other hand, as the increase of the wall-normal height, the negative tail of the p.d.f. of T' decays more slowly, which cannot be recovered by the MSRA family, although the p.d.f. of T_h' is the closest, whereas for the positive tail, the p.d.f.s of T_h', T_g', and T_r' are closer to it. This suggests that the strong negative temperature fluctuations cannot be captured by the MSRA models for the channel flow. The results reported in § 4.1.2 show that the temperature fluctuations at small scales cannot be well depicted by the HSRA. It may imply that the small-scale eddies primarily carry negative strong temperature fluctuations. One can also refer to the instantaneous signals compared in figure 8(*a*) at these wall-normal positions.

In figures 7(*b*), 7(*d*) and 7(*f*), we compare the p.d.f.s of T_l' and T_{mg}' at these three select-ed wall-normal positions. As can be seen, unlike the results associated with the MSRA, the p.d.f.s of T_{mg}' are closer to those of T_l' for the fluctuations with high probabilities of occurrence at all wall-normal positions. Figure 8(*b*) displays their instantaneous signals at three selected wall-normal heights. It is apparent that T_{mg}' is in sync with T_l' below the core region of a channel flow. As T_l' and u_l' are demonstrated to be the components of T' and u' controlled by the mean fields and carried by the energy-containing motions (Cheng & Fu 2024*c*) (see (1.20)), it can be envisioned that it is the small-scale eddies which cause T' and u' to be out of sync beyond the near-wall region, see figure 8(*a*).

Unlike the channel flow, the behaviour of these models in turbulent boundary layers remains nearly unchanged at wall-normal positions far from the extreme point of $\bar{T}$, see figure 1. Hence, we select only one wall-normal locus for analysis. Figures 9(*a*) and 9(*c*) show the p.d.f.s of T_h', T_g' and T_r', along with those of T' obtained from the DNS data at $y/\delta = 0.4$ for M20T100 and M20T050, respectively. The p.d.f. of T_s' is also included in figure 9(*a*) for comparison. For the flow over an adiabatic wall, it is evident that the positive branch of the p.d.f. of T' can be roughly recovered by that of T_g', whereas for its negative branch, the p.d.f. of T_h' is the closest, especially for the fluctuations with high probabilities of occurrence. This scenario can also be traced for the case with a diabatic wall, i.e. M20T050, see figure 9(*c*). However, this is not evident for the channel flow, see figure 7. It underscores the fact that negative and positive temperature fluctuations in compressible turbulent boundary layers establish connections with positive and negative velocity fluctuations in different ways, irrespective of the wall thermal condition. To the
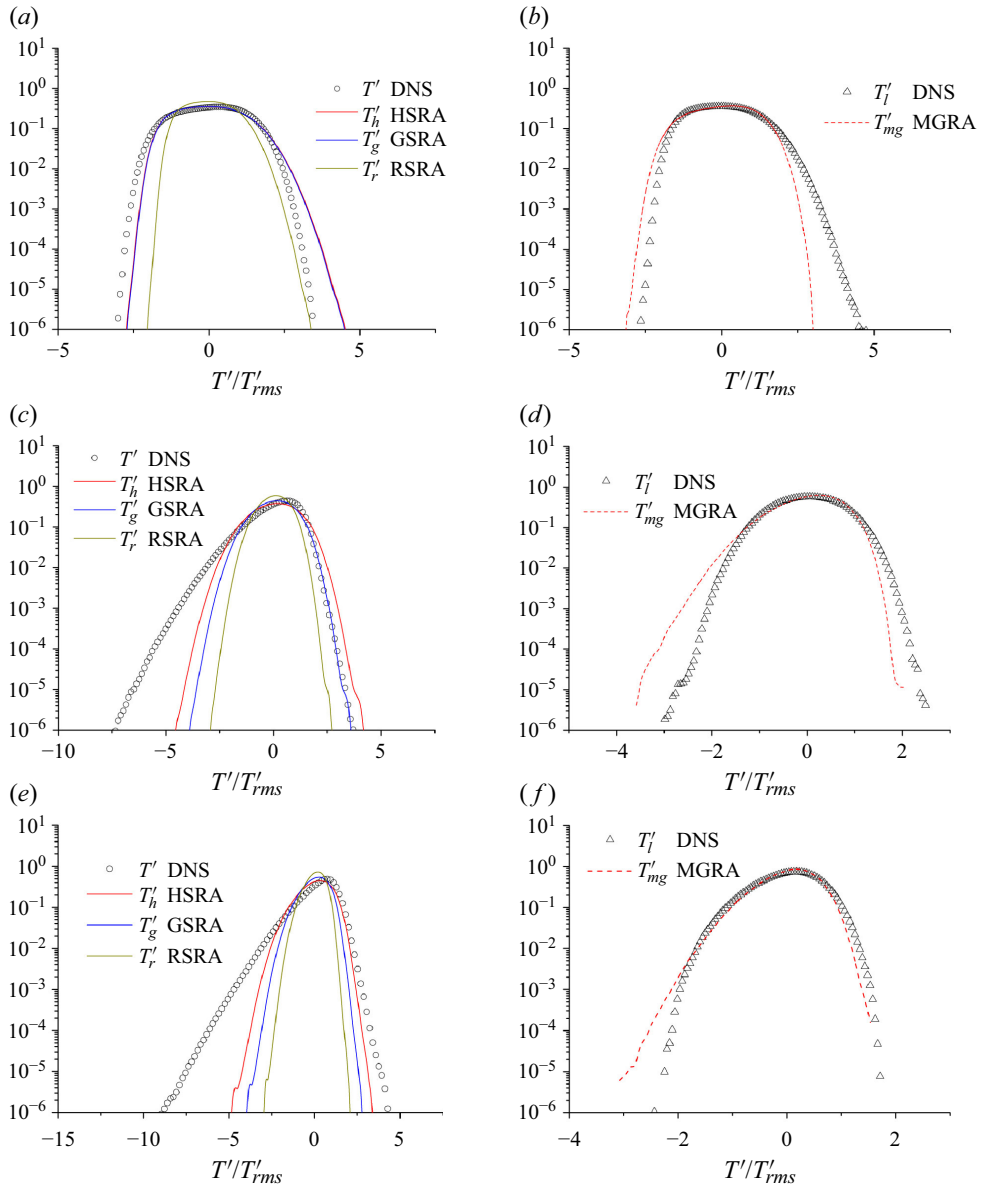
Figure 7. (*a,c,e*) Probability density functions of T_h', T_g' and T_r' at (*a*) $y^* = 10$, (*c*) $y = 0.2h$, (*e*) $y = 0.5h$; (*b,d,f*) p.d.f.s of T_{mg}' at (*b*) $y^* = 10$, (*d*) $y = 0.2h$, (*f*) $y = 0.5h$. A channel case Ma15Re20K is taken into consideration, and the p.d.f.s of T' and T_l' obtained from DNS at each locus are included for comparison.

authors' knowledge, this phenomenon has not been previously reported. Therefore, it may be sensible to describe the relationship between T' and u' in compressible turbulent boundary layers by taking their signs into account. Considering $\partial \bar{T} / \partial \bar{u} < 0$ in the outer region of a compressible boundary layer, it implies that $u' > 0$ and $T' < 0$ are correlated with each other via the HSRA, whereas the relation between $u' < 0$ and $T' > 0$ can be described by the GSRA.
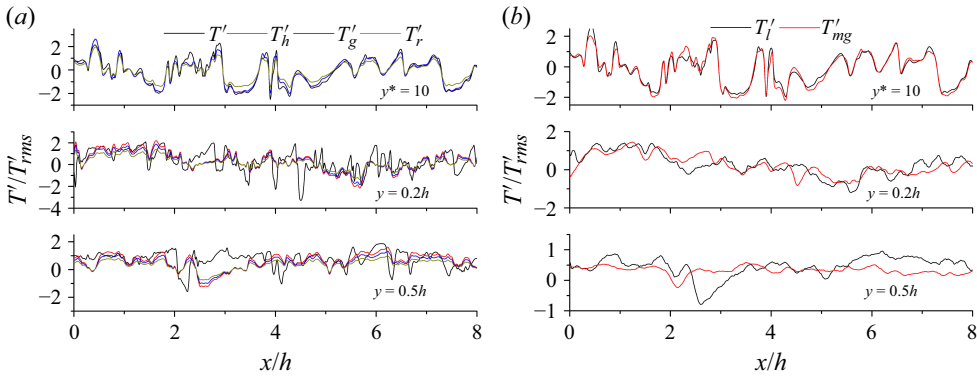
Figure 8. (*a*) Instantaneous signals of T', T'_h, T'_g and T'_r along streamwise direction at $y^* = 10$, $y = 0.2h$ and $y = 0.5h$; (*b*) instantaneous signals of T'_{mg} and T'_l along streamwise direction at $y^* = 10$, $y = 0.2h$ and $y = 0.5h$. A channel case Ma15Re20K is taken into consideration.

To further elucidate this relationship between T' and u', we define two additional ratio functions, which can be cast as

$$r_p = \left(\left| \frac{\partial \bar{T}}{\partial \bar{u}} \right| u'_{rms}|_{u'<0} \right) / T'_{rms}|_{T'>0}, \tag{4.3}$$

$$r_n = \left(\frac{1}{Pr_t} \left| \frac{\partial \bar{T}}{\partial \bar{u}} \right| u'_{rms}|_{u'>0} \right) / T'_{rms}|_{T'<0}. \tag{4.4}$$

Here, r_p and r_n are intended to diagnose the relations between $T' > 0$ and $u' < 0$, and that between $T' < 0$ and $u' > 0$, respectively. Their distributions are illustrated in figure 10. The variations of r_1 for the GSRA and the HSRA are also contained for comparison. It is transparent that in the outer region away from the extreme point of $\bar{T}$, the magnitudes of r_p and r_n are closer to unity for each case, in contrast to those of r_1 related to the HSRA and the GSRA. This highlights the fact that the relation between $T' > 0$ and $u' < 0$ follows the description of the GSRA, while that between $T' < 0$ and $u' > 0$ follows the HSRA in compressible turbulent boundary layers. A single formula cannot accurately describe the relation between T' and u', without taking their signs into account. The reasons for these asymmetric behaviours between positive and negative signals are currently unclear and warrant further investigations in the future. In summary, we suggest a new relation for the compressible wall boundary layer with $\partial \bar{T}/\partial \bar{u} < 0$ (not applicable to the channel flow), which can be expressed in a commonly used from as

$$\frac{\sqrt{\overline{T'^2}}/\bar{T}}{(\gamma - 1)M^2 \sqrt{\overline{u'^2}}/\bar{u}} = \begin{cases} \dfrac{1}{|Pr_t \left(1 - \partial \bar{T}_t/\partial \bar{T}\right)|} & \text{for } u' > 0 \text{ and } T' < 0, \\ \dfrac{1}{|\left(1 - \partial \bar{T}_t/\partial \bar{T}\right)|} & \text{for } u' < 0 \text{ and } T' > 0. \end{cases} \tag{4.5}$$

As an aside, the p.d.f.s of T'_s and T'_h nearly collapse with each other for the case M20T100. It suggests that the performance of the SRA and the HSRA is nearly identical for turbulence over an adiabatic wall. Figures 9(*b*) and 9(*d*) compare the p.d.f.s of T'_l and T'_{mg} at $y/\delta = 0.4$ for these two cases. Apparently, they agree well with each other for the fluctuations with high probabilities of occurrence, just like the scenario in the channel flow, see figure 7(*b,d,f*). The underlying reason is given above and is omitted here.
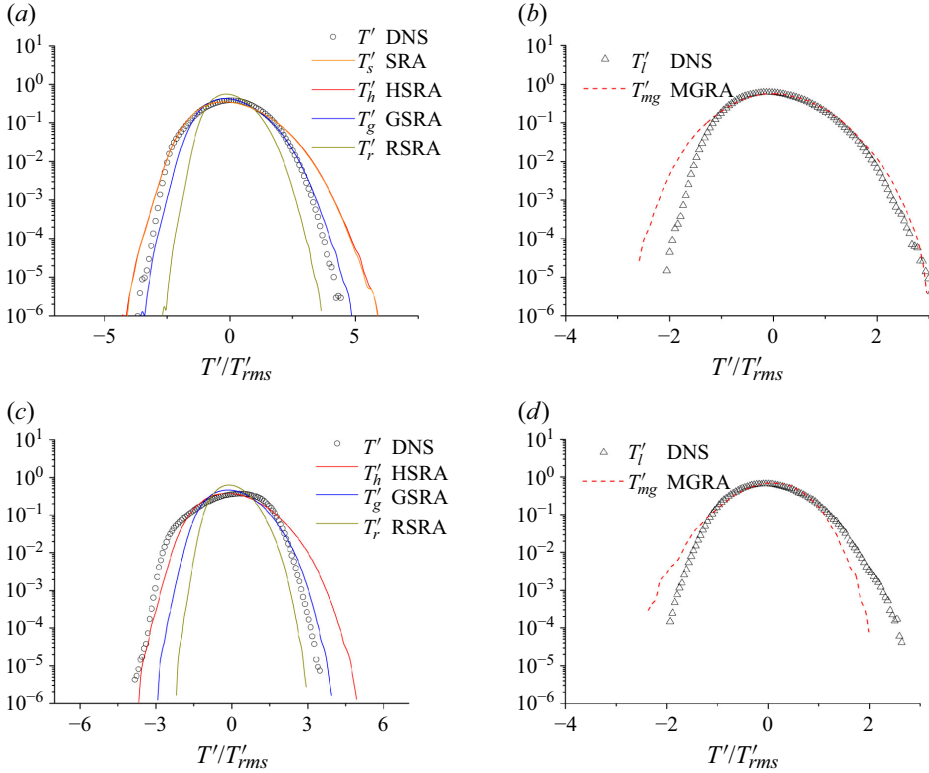
Figure 9. (*a*,*c*) Probability density functions of T', T'_h, T'_g and T'_r at $y = 0.4\delta$ for (*a*) M20T100 and (*c*) M20T050; (*b*, *d*) p.d.f.s of T'_l and T'_{mg} at $y = 0.4\delta$ for (*b*) M20T100 and (*d*) M20T050. In panel (*a*), the p.d.f. of T'_s is also added for comparison.

5. Discussion

5.1. *Phase difference between u' and T'*

Some may wonder whether there is a phase difference between instantaneous u' and T', which affects the performance of the MSRA and MGRA models in capturing the instantaneous characteristics. For example, nearly two decades ago, Xu & Martin (2004) assumed the following relation between the instantaneous u' and T' in compressible turbulent boundary layers:

$$\frac{T'(t)}{T'_{rms}} = c \frac{u'(t + f_{phase})}{u'_{rms}}, \tag{5.1}$$

where t and f_{phase} denote time and frequency difference, respectively, and $c = \pm 1$. The exact value of c is determined by the gradients of $\bar{u}$ and $\bar{T}$. However, they have not examined the existence of f_{phase}. Due to the convection effect, the frequency difference and the space phase difference correspond to each other.

Accordingly, to check whether these differences exist, we can calculate the following cross-correlation:

$$R_{u'T'}(\Delta r; y) = \left| \frac{\langle T'(x, y)u'(x + \Delta r, y)\rangle}{\sqrt{\langle T'^2\rangle\langle u'^2\rangle}} \right|, \tag{5.2}$$

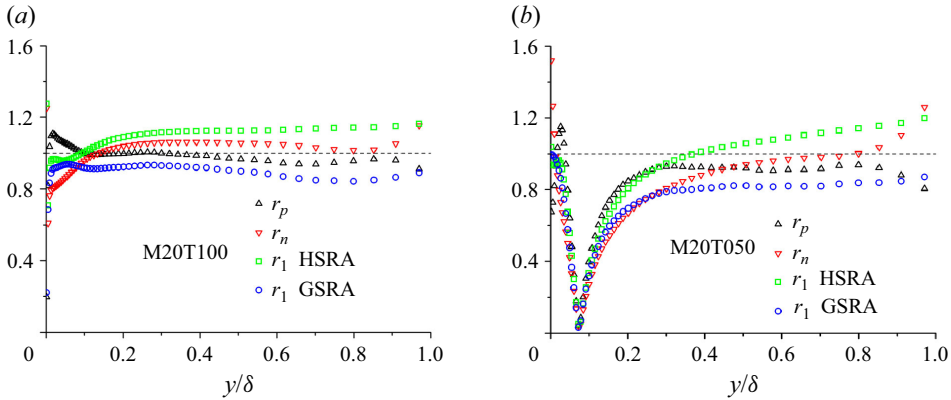Figure 10. (*a,b*) Variations of ratio functions r_p and r_n for (*a*) Ma20T100 and (*b*) Ma20T050. The distributions of r_1 related to the HSRA and the GSRA for each case are also shown for comparison in each panel.
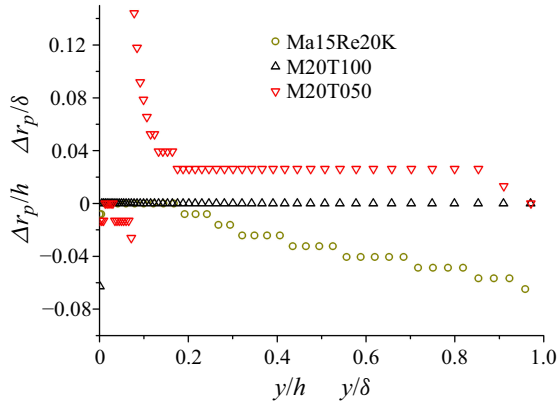

Figure 11. Variations of $\Delta r_p / h$ ($\Delta r_p / \delta$) as functions of wall-normal height for the cases Ma15Re20K, M20T100 and M20T050.

where Δr denotes the streamwise delay. If $\Delta r_p \approx 0$, it suggests that the phase difference between them is negligible at a given y. Here, Δr_p denotes the streamwise delay corresponding to the peak in $R_{u'T'}$. Figure 11 displays the variations of $\Delta r_p / h$ ($\Delta r_p / \delta$) as functions of wall-normal height for the cases Ma15Re20K, M20T100 and M20T050. For the channel flow Ma15Re20K, $\Delta r_p / h$ decreases from 0 in the near-wall region to a small value –0.03 at $y/h = 0.5$ (approximately three streamwise grid spacings) and –0.06 in the channel centre (approximately seven streamwise grid spacings). For the flow over an adiabatic wall M20T100, $\Delta r_p / \delta$ remains zero across the whole boundary layer, whereas for the flow with a cold wall M20T050, $\Delta r_p / \delta$ is only significant around the extreme point of $\bar{T}$ and tends to keep a small value for $y > 0.2\delta$ (approximately two streamwise grid spacings). The deviation around the extreme point of $\bar{T}$ is acceptable, because u' and T' are decorrelated near this zone. All in all, these observations bring to the fore the negligible effect of the phase difference between the instantaneous u' and T' in most regions of a flow, as $\Delta r_p / h$ ($\Delta r_p / \delta$) are of small magnitudes in most wall-normal positions. In the core region of an internal flow, the influences of the acoustic mode are non-negligible (Chen *et al.* 2023*b*; Xu *et al.* 2023; Cheng & Fu 2024*b*). As a result, the phase difference

between u' and T' in the core region of a channel flow is larger than that of a boundary layer, although its magnitude is not that large within the case under scrutiny.

5.2. *Relationship between small-scale temperature and velocity fluctuations*

The above elaborate analyses indicate that the HSRA is the only model in the MSRA family that works well for both the channel flow and the turbulent boundary layer in the statistical sense. Furthermore, the MGRA is also shown to be effective in describing the intrinsic duality relation between u'_l and T'_l tied by the mean fields and the energy-containing motions, regardless of the geometry of flow. Accordingly, combining these two relations, namely (1.7) and (1.21), and using $\overline{u'_l u'_{nl}} = 0$ and $\overline{t'_l t'_{nl}} = 0$ (these two relations are verified by analysing the present database, and not shown here for brevity), we can derive a formula that depicts the statistical relation between the small-scale components of these two fields (u'_{nl} and T'_{nl})

$$\frac{T'_{nl,rms}}{u'_{nl,rms}} = \left| \frac{\partial \bar{T}}{\partial \bar{u}} \right| \sqrt{\frac{\overline{u'^2_l}}{\overline{u'^2_{nl}}} \left[\left(\frac{1}{Pr_t} \right)^2 - 1 \right] + \left(\frac{1}{Pr_t} \right)^2}. \tag{5.3}$$

If $Pr_t = 1$, (5.3) becomes $T'_{nl,rms} = |(\partial \bar{T}/\partial \bar{u})| u'_{nl,rms}$. This observation implies that the deviation of Pr_t from unity results in a complicated relationship between the small-scale components of these two fields. Numerous studies have reported the modelling of the distribution of Pr_t, hence our focus of analyses below is the modelling of the ratio term $\overline{u'^2_l}/\overline{u'^2_{nl}}$.

Figures 12(*a*) and 12(*b*) show the distributions of $\overline{u'^2_l}/\overline{u'^2_{nl}}$ for all channel flows and boundary layers considered in the present study, respectively. Significant differences can be observed in the near-wall region, owing to the distinct wall thermal boundary condition of each case. However, for the turbulent boundary layers, the magnitude of this ratio for each case converges to a constant with increasing wall-normal height, even in the outer layer, that is, $\overline{u'^2_l}/\overline{u'^2_{nl}} \approx 1.2$. In this regard, $\overline{u'^2_l}/\overline{u'^2_{nl}} = 1.2$ is the simplest model of this term for turbulent boundary layers. For the channel flows, its value decays beyond the near-wall region and is nearly Mach-number independent, which can be fitted to be $\overline{u'^2_l}/\overline{u'^2_{nl}} = \exp(0.86 - 2.3y/h) \equiv g(y)$. Accordingly, (5.3) can be simplified as

$$\frac{T'_{nl,rms}}{u'_{nl,rms}} = \left| \frac{\partial \bar{T}}{\partial \bar{u}} \right| \sqrt{(g(y) + 1) \left(\frac{1}{Pr_t} \right)^2 - g(y)}, \tag{5.4}$$

for channel flows. For turbulent boundary layers, it becomes

$$\frac{T'_{nl,rms}}{u'_{nl,rms}} = \left| \frac{\partial \bar{T}}{\partial \bar{u}} \right| \sqrt{2.2 \left(\frac{1}{Pr_t} \right)^2 - 1.2}. \tag{5.5}$$

As long as $Pr_t < 1$, it can be proved from (5.4) and (5.5) that $(T'_{nl,rms}/u'_{nl,rms}) > (1/Pr_t)|(\partial \bar{T}/\partial \bar{u})| > |(\partial \bar{T}/\partial \bar{u})| > (1/1.34)|(\partial \bar{T}/\partial \bar{u})|$. This is consistent with the observations reported in §4.1.2 that the intensity of small-scale T' with respect to that of u' is larger than the predictions of the MSRA models under consideration. It bears emphasising that, although the variations of $\overline{u'^2_l}/\overline{u'^2_{nl}}$ are different in channel flows and boundary layers, they are all Mach-number independent in the outer region. The underlying mechanisms of this phenomenon deserve further investigations in future study.
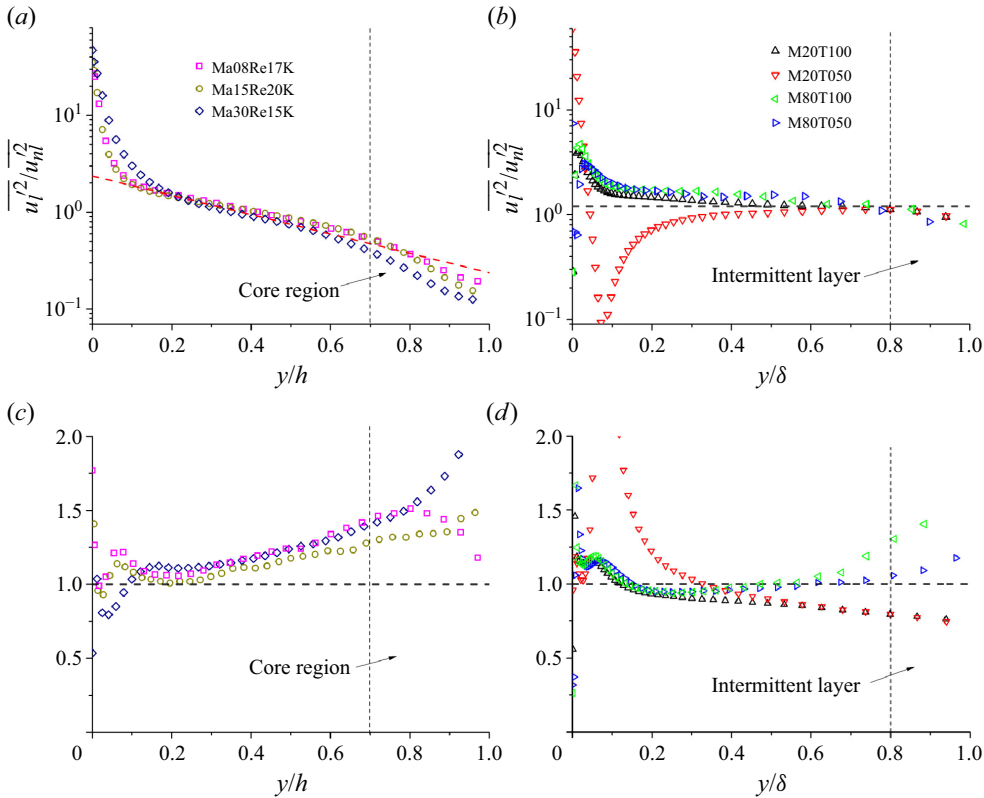
Figure 12. (*a*,*b*) Distributions of $\overline{u_l'^2}/\overline{u_{nl}'^2}$ for (*a*) channel flows and (*b*) turbulent boundary layers; (*c*,*d*) distributions of the ratios of the left-hand term to the right-hand term of (5.4) and (5.5) for (*c*) channel flows and (*d*) turbulent boundary layers. The red dashed line in panel (*a*) denotes $\overline{u_l'^2}/\overline{u_{nl}'^2} = \exp(0.86 - 2.3y/h)$, and the transverse dashed line in panel (*b*) denotes $\overline{u_l'^2}/\overline{u_{nl}'^2} = 1.2$.

Figures 12(*c*) and 12(*d*) display the distributions of the ratios of the left-hand term to the right-hand term of (5.4) and (5.5) for all cases. Note that, the Pr_t in each formula is calculated from DNS. Apparently, (5.4) and (5.5) provide a reasonable description for the intensities of the small-scale temperature and velocity fluctuations within broad wall-normal regions for each type of flow. The errors may be ascribed to the inaccuracy of the HSRA in the intermittent layer of a boundary layer and the core region of a channel flow (see figure 1*a*,*c*,*e*).

5.3. *Spectral models for $u' - T'$ relation*

We can still go further. To be specific, we can also demarcate the spectral regions where (1.21), (5.4) and (5.5) hold. To this end, the 1-D LCS introduced in § 3 is employed. Note that in previous studies, we inspected the $u' - T'$ coupling in an $x-z$ plane with the aid of the 2-D LCS (Cheng & Fu 2023, 2024*a*,*b*). For the 2-D LCS, the linear coherence is shown as a function of λ_x and λ_z simultaneously, which is not as simple as that of a 1-D LCS for modelling purposes. Additionally, the 2-D LCS is not suitable for displaying changes in coherence along the wall-normal direction. Hence, we resort to the 1-D LCS in the present study.
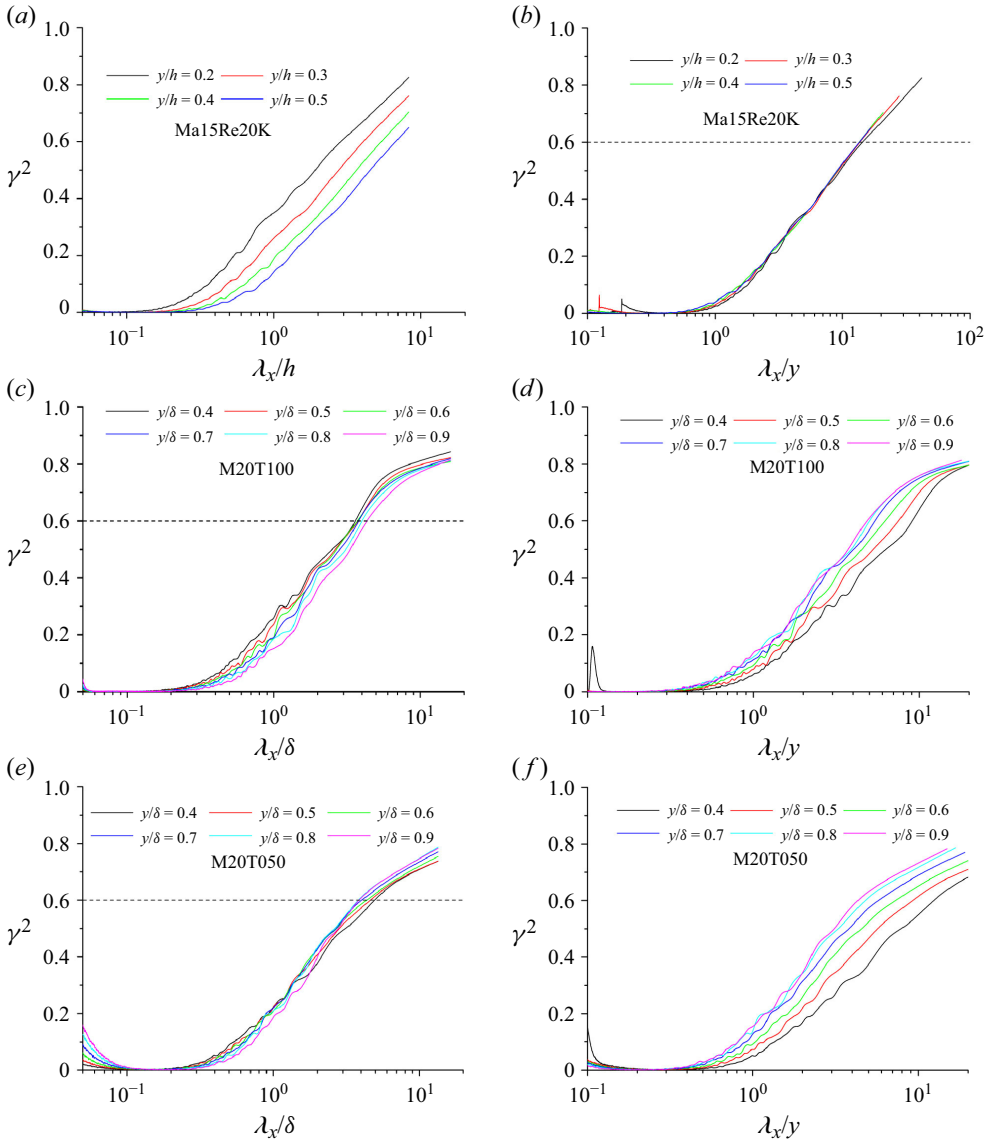
Figure 13. (a,c,e) Variations of $\gamma^2(\lambda_x; y)$ for (a) a turbulent channel flow Ma15Re20K, (c) a boundary layer with an adiabatic wall M20T100 and (e) a boundary layer with a cold wall M20T050 with λ_x scaled by the outer scale at several selected wall-normal positions; (b,d,f) variations of $\gamma^2(\lambda_x; y)$ for (b) a turbulent channel flow Ma15Re20K, (d) a boundary layer with an adiabatic wall M20T100 and (f) a boundary layer with a cold wall M20T050 with λ_x scaled by the wall-normal heights at several selected wall-normal positions.

Figure 13 shows the variations of $\gamma^2(\lambda_x; y)$ as functions of λ_x at some selected wall-normal locations for several cases. In figure 13(a,c,e), λ_x is scaled by the outer scale, namely h or δ, whereas in figure 13(b,d,f), λ_x is scaled by the corresponding wall-normal height y. For the turbulent channel flow Ma15Re20K, the profiles of γ^2 do not agree with each other if λ_x is scaled by the outer scale. However, when λ_x is scaled by the wall-normal height, the profiles collapse well. It implies that the wall-normal height is the characteristic length scale of the $u' - T'$ coupling in a turbulent channel flow. Interestingly, this scenario is reversed for turbulent boundary layers, see figure 13($c-f$). It can be observed that the

distributions of $\gamma^2(\lambda_x; y)$ match fairly well with each other if they are plotted against λ_x/δ (see figure 13c,e). On the contrary, these profiles are scattered when λ_x is scaled by y (see figure 13d, f). This observation highlights the fact that the outer scale is the key parameter in shaping the $u' - T'$ coupling in compressible turbulent boundary layers, which is in stark contrast to that of a channel flow. We conjecture that it is the geometry of the flow that results in this difference. It is well known that there is no obvious wake region in an internal flow (Trettel & Larsson 2016; Griffin *et al.* 2021). In this regard, its outer region can be regarded as an extension of the logarithmic region where the flow properties are characterised by the wall-normal height. On the contrary, the wake region is a pivotal part of a boundary layer, where the characteristic length scale is δ. This also gives an explanation for the distinct variation tendencies of velocity and temperature correlations (i.e. $C_{u'T'}$ defined by (1.3)) in turbulent channel flows and turbulent boundary layers, which have been widely reported in numerous studies. The magnitude of $C_{u'T'}$ in a channel flow is attenuated with increasing wall-normal height (see figure 2c of Cheng & Fu 2023), whereas for a compressible boundary layer, $C_{u'T'}$ maintains around -0.6 in the wake region (see figure 17 of Cogo *et al.* 2023), irrespective of the wall thermal condition and free-stream Mach number.

The well-established scalings exhibited in figure 13 can serve as a cornerstone for tracking the spectral boundaries of the deduced relations (1.21), (5.4) and (5.5). Through trial and error, we find that $\gamma^2(\lambda_x; y) = 0.6$ is a suitable condition for determining the spectral range affected by energy-containing motions for both these two types of wall turbulence. Correspondingly, it is expected to coincide with $\lambda_x^\star = 14y$ and $\lambda_x^\star = 4\delta$ for a channel flow and a turbulent boundary layer, respectively (see the dashed lines figure 13). Herein, we use $\lambda_x^\star$ to represent the streamwise length scale corresponding to the spectral boundary. Interestingly, the first value represents the streamwise length scale of the self-similar energy-containing motions at a given wall-normal height in both incompressible and compressible flows (Baars *et al.* 2017; Baars & Marusic 2020; Cheng & Fu 2022), and the latter is believed to be the spectral length boundary between the large-scale and very-large-scale motions in the wake region of a boundary layer (Hutchins & Marusic 2007; Smits *et al.* 2011). To further appraise the accuracy of these determined $\lambda_x^\star$, we defined the following two metrics, which take the form of:

$$r_4 = \left(\left| \frac{\partial \bar{T}}{\partial \bar{u}} \right| u'_{rms}|_{\lambda_x > \lambda_x^\star} \right) / T'_{rms}|_{\lambda_x > \lambda_x^\star}, \tag{5.6}$$

and

$$r_5 = \left(\left| \frac{\partial \bar{T}}{\partial \bar{u}} \right| \sqrt{\frac{\overline{u_l'^2}}{\overline{u_{nl}'^2}} \left[\left(\frac{1}{Pr_t} \right)^2 - 1 \right] + \left(\frac{1}{Pr_t} \right)^2} \, u'_{rms}|_{\lambda_x < \lambda_x^\star} \right) / T'_{rms}|_{\lambda_x < \lambda_x^\star}, \tag{5.7}$$

where $u'_{rms}|_{\lambda_x > \lambda_x^\star}$ denotes the intensity of streamwise velocity fluctuations at scales $\lambda_x > \lambda_x^\star$ for a given wall-normal height. The meanings of other symbols with similar subscripts can be inferred by analogy. For turbulent boundary layers and channel flows, $\overline{u_l'^2}/\overline{u_{nl}'^2}$ is modelled as 1.2 and $g(y)$, respectively. If the chosen $\lambda_x^\star$ accurately demarcates the spectral regions where (1.21), (5.4) and (5.5) hold, the magnitudes of r_4 and r_5 should be approximately equal to one.

Figure 14 shows the variations of r_4 and r_5 for all these cases. For the channel flows, due to the limitation of the size of the computational domain for each case, we only show the values of r_4 and r_5 below the core region. It can be observed that the magnitudes of r_4 of channel flows are close to unity for $y/h < 0.5$, as well as those of r_5. For turbulent
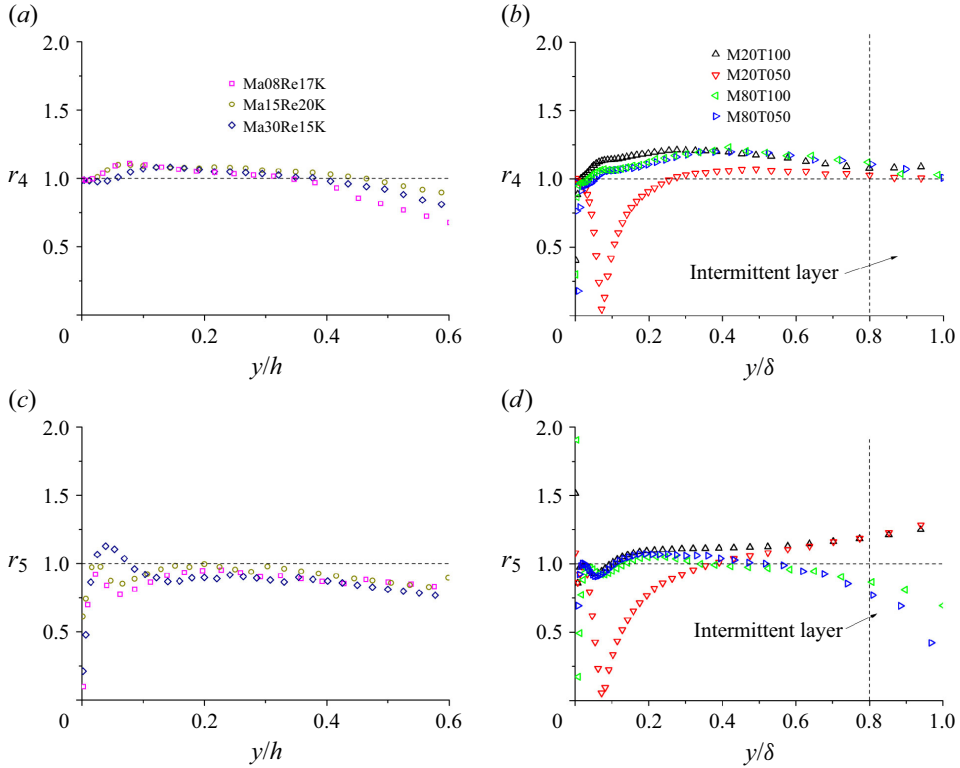
Figure 14. (*a*,*b*) Distributions of r_4 for (*a*) channel flows and (*b*) turbulent boundary layers; (*c*,*d*) distributions of r_5 for (*c*) channel flows and (*d*) turbulent boundary layers.

boundary layers, the magnitudes of r_4 and r_5 for all cases are also close to unity below the intermittent layer ($y/\delta < 0.8$). We have checked that choosing $\lambda_x^\star$ based on $\gamma^2(\lambda_x; y) = 0.4$ or $\gamma^2(\lambda_x; y) = 0.5$ yields similar results. Hence, the following models describing the $u' - T'$ relation in spectral space can be established: for a channel flow:

$$\frac{T'_{rms}(\lambda_x; y)}{u'_{rms}(\lambda_x; y)} = \begin{cases} \left|\dfrac{\partial \bar{T}}{\partial \bar{u}}\right| \sqrt{(g(y) + 1)\left(\dfrac{1}{Pr_t}\right)^2 - g(y)} & \text{for } \lambda_x < 14y, \\ \left|\dfrac{\partial \bar{T}}{\partial \bar{u}}\right| & \text{for } \lambda_x > 14y, \end{cases} \tag{5.8}$$

and for a compressible boundary layer

$$\frac{T'_{rms}(\lambda_x; y)}{u'_{rms}(\lambda_x; y)} = \begin{cases} \left|\dfrac{\partial \bar{T}}{\partial \bar{u}}\right| \sqrt{2.1\left(\dfrac{1}{Pr_t}\right)^2 - 1.1} & \text{for } \lambda_x < 4\delta, \\ \left|\dfrac{\partial \bar{T}}{\partial \bar{u}}\right| & \text{for } \lambda_x > 4\delta. \end{cases} \tag{5.9}$$

The statistical validity of the HSRA in channel flows and boundary layers results from the cumulative effects of these multi-scale eddies. We will further examine our models as more data at different Mach numbers and Reynolds numbers are collected in the future.

It also bears reiterating that there are several factors that can affect the accuracy of these formulas. Firstly, their establishments depend on the accuracy of the MGRA

1017 A34-26

and the HSRA. Our previous study demonstrated that the MGRA is Reynolds-number dependent and is more accurate for flows with high Reynolds numbers (Cheng & Fu 2024*c*), moreover, the accuracy of the HSRA is also attenuated in the core region of a channel flow (Huang *et al.* 1995; Brun *et al.* 2008) and the intermittent layer of a boundary layer (Zhang *et al.* 2018; Huang *et al.* 2022). Secondly, the modelling of $\overline{u_l'^2}/\overline{u_{nl}'^2}$ for each type of flow is only valid beyond the near-wall region, see figure 12; thirdly, actually, the variations of ϵ_T and ϵ_{Tl} with increasing λ_x at a given y in the outer region of each case are continuous. As a consequence, (5.8) and (5.9) are only rough estimations.

One may ask: Can scale separation be performed along the spanwise length scale λ_z to construct another generic spectral model, in addition to that related to λ_x? In Appendix B, we display the variations of $\gamma^2(\lambda_z; y)$ for all the flows considered at several selected wall-normal heights. Their distribution characteristics indicate that λ_z is not a good choice for constructing a spectral model; see the related discussions in Appendix B.

5.4. *A strategy for generating more reliable temperature fluctuations as the inlet boundary condition for DNS/LES of compressible boundary layers*

As mentioned in the introduction, one of the most common applications of the Reynolds analogy models is to generate the instantaneous temperature fluctuations given known streamwise velocity fluctuations and mean fields ($\bar{u}$ and $\bar{T}$). The generated fields can be deployed for the construction of the inlet boundary condition for the DNS/LES of compressible turbulent boundary layers. For example, Martin (2007) and Mo *et al.* (2023) appealed to the SRA and the GSRA to achieve this for the simulations of the supersonic boundary layers with adiabatic walls, respectively. It is worth mentioning that a physically consistent inlet boundary condition is conducive to shortening the transition process from the inflow to the fully developed turbulence downstream, which is commonly referred to as the recovery distance.

In § 4.1.3, we are dedicated to appraising the state-of-the-art MSRA models for describing the instantaneous relationship between T' and u'. Our analyses indicate that using a single formula to depict it is somewhat arbitrary. Instead, it is judicious to consider the relations between $T' > 0$ and $u' < 0$, and between $T' < 0$ and $u' > 0$, separately. According to the results displayed above, the following relationship is more suitable for generating the instantaneous temperature fluctuation field for compressible boundary layers:

$$
T'_\star =
\begin{cases}
\dfrac{1}{Pr_t}\dfrac{\partial \bar{T}}{\partial \bar{u}} u' & \text{for } u' \ge 0, \\[2ex]
\dfrac{\partial \bar{T}}{\partial \bar{u}} u' & \text{for } u' < 0.
\end{cases}
\tag{5.10}
$$

Here, we use subscript '$\star$' to distinguish it from previously defined temperature fluctuations from the MSRA family and the MGRA in § 4.1.3.

Under normal circumstances, the distribution of Pr_t is not known in advance. In light of this, one can use the empirical formula given by Subbareddy & Candler (2012) for the supersonic boundary layer, $Pr_t = 1 - 0.25y/\delta$. Of course, a simpler and more commonly used expression, $Pr_t = 0.9$, can also be adopted. Furthermore, for supersonic and hypersonic boundary layers with distinct wall thermal conditions, $\partial \bar{T}/\partial \bar{u} < 0$ is well established beyond the log region ($y/\delta > 0.2$), which suggests that the correspondence between T' and u' with different signs reported above is broadly true. In figure 15, we compare the ratio of the root-mean-square values of $T'_\star$ and T' obtained from DNS data. Apparently, (5.10) with either introduced model of Pr_t is more accurate than the single-formula HSRA and GSRA models, and the model $Pr_t = 1 - 0.25y/\delta$ works better. The superiority of the new
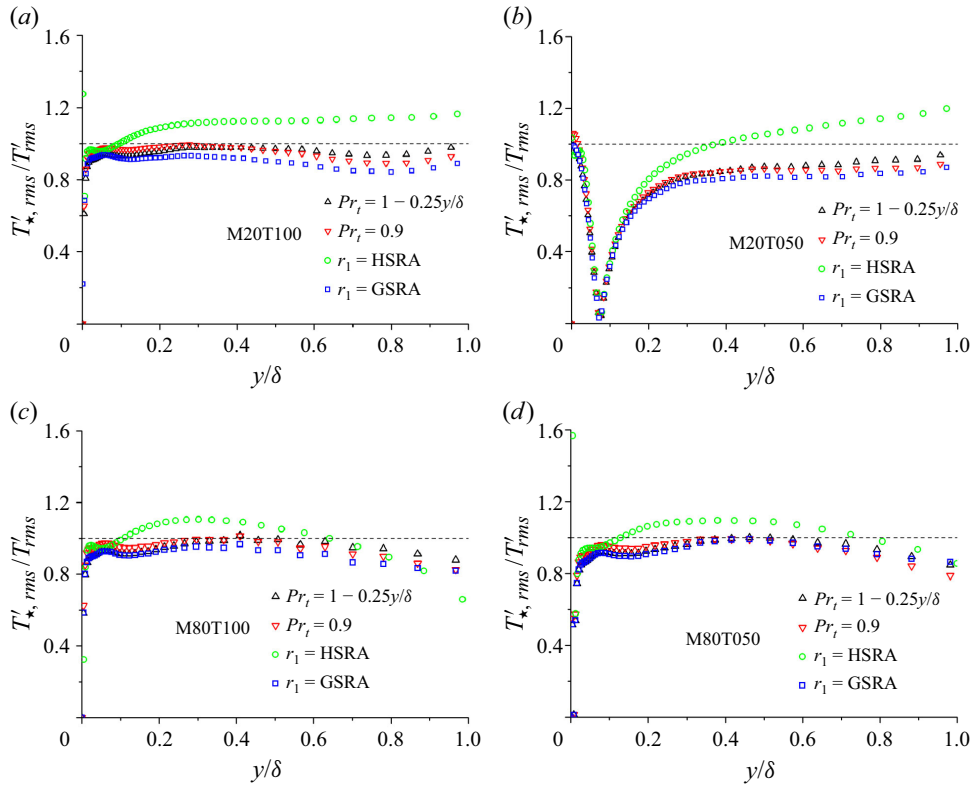
Figure 15. The ratio between the root-mean-square values of $T'_\star$ and T' for all cases of turbulent boundary layer with different modellings of Pr_t, and the variations of r_1 related to the HSRA and the GSRA are added for comparison. The dashed lines in panels denote $T'_{\star,rms}/T'_{rms} = 1$.

formula (5.10) for flows with adiabatic walls is more apparent. It is noted that the eddies in the inner layer are regenerated rapidly, making it unnecessary to treat them with a high degree of accuracy at the inlet (Spalart *et al.* 2006). Hence, for a turbulent boundary layer with a diabatic wall, although $T'_\star$ cannot exactly recover T' near the zone adjacent to the extreme point of $\bar{T}$, which is located in the near-wall region, its accuracy in the outer region (see figures 15*b* and 15*d*) can still help reduce the recovery distance. We will further assess the accuracy of this method when sufficient data are available.

6. Concluding remarks

In the present study, we broadly investigate the relation between T' and u' in compressible channel flows and turbulent boundary layers with distinct wall thermal conditions and Mach numbers, through assessing the state-of-the-art Reynolds analogy models from three perspectives, specifically, in the statistical sense, in spectral space and via the distribution characteristics of T'. The key findings are summarised below.

(i) Among the MSRA family, the HSRA is the only model that works well for both these two types of flows in the statistical sense. By contrast, the GSRA performs poorly in channel flows, whereas the RSRA is the worst, performing poorly in any flow. The accuracy of the GSRA depends on wall temperature and the geometry of the flow.
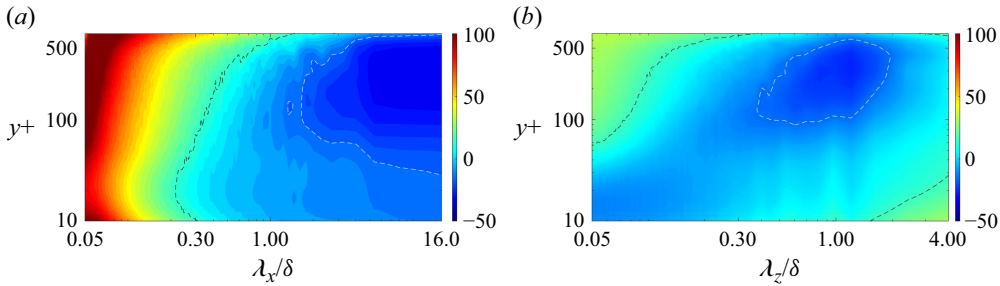
Figure 16. Distributions of the error function ϵ_T with respect to (*a*) streamwise and (*b*) spanwise length scales for the SRA. A turbulent boundary layer case with an adiabatic wall M20T100 is taken into consideration. The value in each panel is expressed as a percentage count. The black and white dashed lines in panels are 15 % and −15 % isolines, respectively.

(ii) In spectral space, the intensities of T' at small scales are discovered to be larger than the predictions given by the MSRA family, whereas those at scales corresponding to the energy-containing eddies and the large-scale motions are approximately equal to and less than the predictions of the HSRA, respectively. The success of the HSRA is the outcome of this combined effect. Furthermore, the MGRA accurately describes the relationship between the large-scale T' and u' that are dictated by the mean fields and the energy-containing motions.

(iii) The scales of T'_l and u'_l correspond to the scales of energy-containing eddies, and their distribution characteristics exhibit significant similarities. Their relation can be well described by the MGRA. The presence of small-scale fluctuations in T' and u' obscures this similarity. It is also observed that there is no significant space phase difference between T' and u' at a given wall-normal position for each kind of flow.

(iv) In compressible turbulent boundary layers, the relationship between the intensities of positive temperature and negative velocity fluctuations can be described by the GSRA, whereas that between negative temperature and positive velocity fluctuations is accurately depicted by the HSRA. This finding can be used to construct a more accurate inlet temperature boundary condition for the DNS/LES of compressible boundary layers.

(v) The streamwise length scale, rather than the spanwise length scale, is found to be more suitable for characterising the scale characteristics of $u' - T'$ coupling in spectral space. For channel flows and boundary layers, the scale boundaries of the coupling resulting from the small-scale and energy-containing motions can be represented by $\lambda_x = 14y$ and $\lambda_x = 4\delta$ beyond the near-wall region, respectively. Based on this, models describing the relations between T' and u' in spectral space for channel flows and boundary layers are developed.

The present study highlights the fact that the $u' - T'$ coupling at small scales is beyond the predictive capabilities of existing models. Therefore, the next urgent issue to address is the relationship between the velocity fluctuations at small scales and those at scales corresponding to the energy-containing motions, as well as that of temperature fluctuations. This will help in establishing a more accurate Reynolds analogy model. On the other hand, as the Mach number increases, the compressibility effect plays an increasingly important role in the turbulence dynamics. As a result, the temperature field cannot be completely treated as a passive scalar. This may influence the accuracy of a Reynolds analogy model, and requires further investigations in future studies.
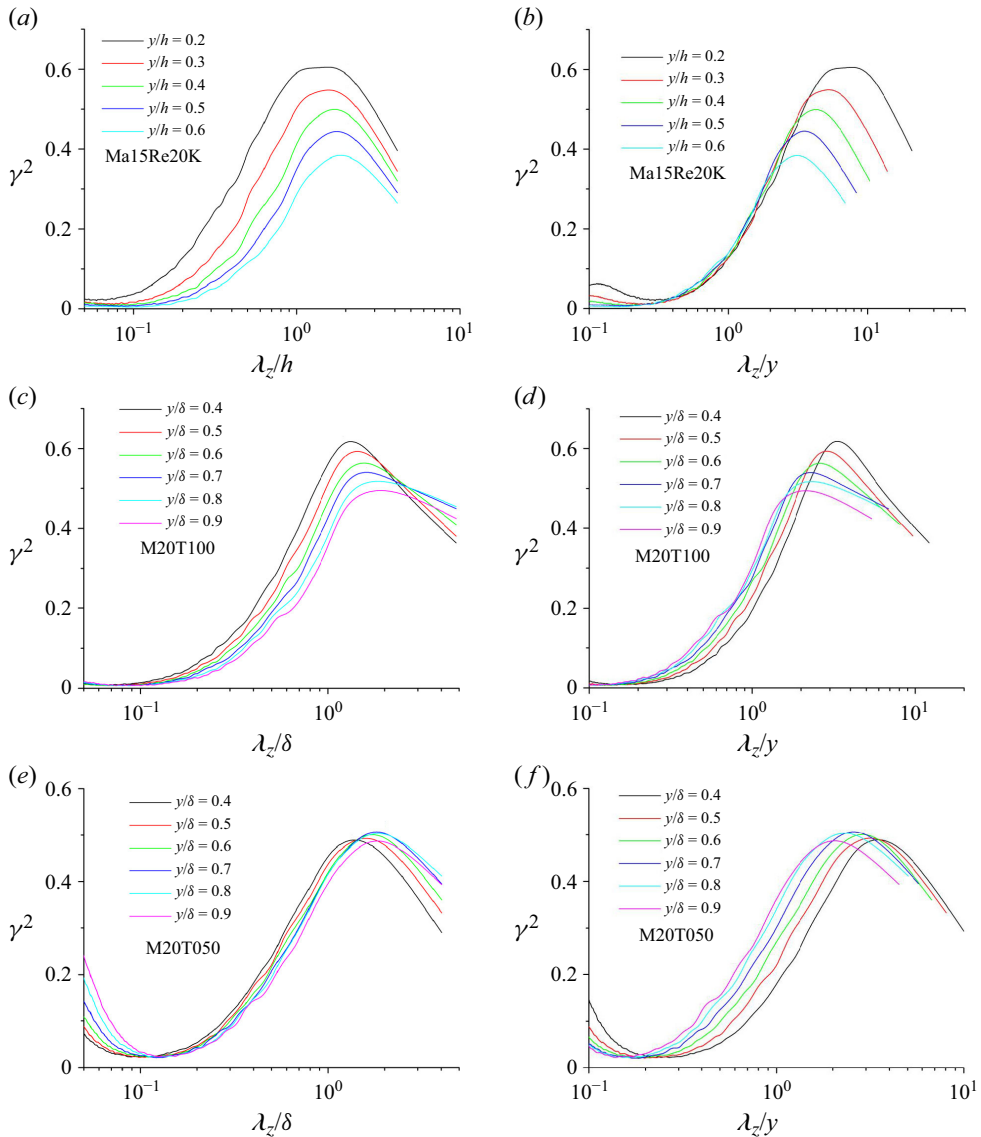
Figure 17. (*a,c,e*) Variations of $\gamma^2(\lambda_z; y)$ for (*a*) a turbulent channel flow Ma15Re20K, (*c*) a boundary layer with an adiabatic wall M20T100 and (*e*) a boundary layer with a cold wall M20T050 with λ_z scaled by the outer scale at several selected wall-normal positions; (*b,d,f*) variations of $\gamma^2(\lambda_z; y)$ for (*b*) a turbulent channel flow Ma15Re20K, (*d*) a boundary layer with an adiabatic wall M20T100 and (*f*) a boundary layer with a cold wall M20T050 with λ_z scaled by the wall-normal heights at several selected wall-normal positions.

1017 A34-30

Appendix A. Spectral error of the SRA for the case M20T100

As a sanity check, we also examine the spectral error of the original SRA, i.e. (1.2), in this appendix for the case M20T100, as previous studies reported that the statistical version of it is satisfied with the experiments and DNSs for flows over adiabatic walls. The error function in spectral space (ϵ_T) takes the form of

$$\epsilon_T = \frac{RS_{uT} - f_0}{f_0} \times 100\,\%. \tag{A1}$$

As can be seen, the spectral diagrams are rather similar to those of the HSRA shown in figures 4(*a*) and 4(*b*). It implies that for this kind of flow, the behaviour of the SRA and the HSRA is rather similar in spectral space.

Appendix B. Variations of $\gamma^2(\lambda_z; y)$ for different kinds of flows

We plot the variations of $\gamma^2(\lambda_z; y)$ as functions of λ_z/h (λ_z/δ) and λ_z/y in figure 17. As can be seen, all profiles of $\gamma^2(\lambda_z; y)$ exhibit non-monotonic behaviour. For turbulent channel flows, the profiles of $\gamma^2(\lambda_z; y)$ at various wall-normal locations agree well with each other for $\lambda_z < 2y$ when plotted against λ_z/y. This is consistent with the streamwise LCS. Even so, they do not match well for $\lambda_z > 2y$. On the other hand, for turbulent boundary layers, normalising λ_z with neither outer scale nor wall-normal height can obtain a fair collapse. This signifies that λ_z is not an appropriate scale parameter in characterising the linear coupling between u' and T' for these two types of canonical compressible wall turbulence as a combination. It may be attributed to the fact that $u' - T'$ coupling is largely mediated by the elongated velocity and temperature streaks in wall turbulence, which are characterised by their streamwise length scales (Chen *et al.* 2023*a*; Cheng & Fu 2023).

REFERENCES

BAARS, W.J., HUTCHINS, N. & MARUSIC, I. 2017 Self-similarity of wall-attached turbulence in boundary layers. *J. Fluid Mech.* **823**, R2.

BAARS, W.J. & MARUSIC, I. 2020 Data-driven decomposition of the streamwise turbulence kinetic energy in boundary layers. Part 1. Energy spectra. *J. Fluid Mech.* **882**, A25.

BAARS, W.J., HUTCHINS, N. & MARUSIC, I. 2016 Spectral stochastic estimation of high-Reynolds-number wall-bounded turbulence for a refined inner-outer interaction model. *Phys. Rev. Fluids* **1** (5), 054406.

BENDAT, J.S. & PIERSOL, A.G. 2011 *Random Data: Analysis and Measurement Procedures*. John Wiley & Sons.

BERNARDINI, M., MODESTI, D., SALVADORE, F. & PIROZZOLI, S. 2021 STREAmS: a high-fidelity accelerated solver for direct numerical simulation of compressible turbulent flows. *Comput. Phys. Commun.* **263**, 107906.

BRUN, C., PETROVAN, B.M., HABERKORN, M. & COMTE, P. 2008 Large eddy simulation of compressible channel flow. *Theor. Comput. Fluid Dyn.* **22** (3), 189–212.

BUSEMANN, A. 1931 *Handbuch Der Experimentalphysik*. vol. 4. Geest und Portig.

CEBECI, T. & SMITH, A.M.O. 1974 *Analysis of Turbulent Boundary Layers*. Academic.

CHEN, X., CHENG, C., FU, L. & GAN, J. 2023*a* Linear response analysis of supersonic turbulent channel flows with a large parameter space. *J. Fluid Mech.* **962**, A7.

CHEN, X., CHENG, C., GAN, J. & FU, L. 2023*b* Study of the linear models in estimating coherent velocity and temperature structures for compressible turbulent channel flows. *J. Fluid Mech.* **973**, A36.

CHEN, X., GAN, J. & FU, L. 2024 An improved Baldwin–Lomax algebraic wall model for high-speed canonical turbulent boundary layers using established scalings. *J. Fluid Mech.* **987**, A7.

CHENG, C., CHEN, X., ZHU, W., SHYY, W. & FU, L. 2024 Progress in physical modeling of compressible wall-bounded turbulent flows. *Acta Mechanica Sin.* **40** (1), 323663.

CHENG, C. & FU, L. 2022 Large-scale motions and self-similar structures in compressible turbulent channel flows. *Phys. Rev. Fluids* **7** (11), 114604.

CHENG, C. & FU, L. 2023 Linear-model-based study of the coupling between velocity and temperature fields in compressible turbulent channel flows. *J. Fluid Mech.* **964**, A15.

CHENG, C. & FU, L. 2024*a* Comparisons between the first- and second-order spectral stochastic estimations in investigating the multiphysics couplings for a supersonic turbulent channel flow. *Phys. Rev. Fluids* **9**, 104607.

CHENG, C. & FU, L. 2024*b* On the streamwise velocity, temperature and passive scalar fields in compressible turbulent channel flows: a viewpoint from multiphysics couplings. *J. Fluid Mech.* **983**, A38.

CHENG, C. & FU, L. 2024*c* A Reynolds analogy model for compressible wall turbulence. *J. Fluid Mech.* **999**, A20.

COGO, M., BAÙ, U., CHINAPPI, M., BERNARDINI, M. & PICANO, F. 2023 Assessment of heat transfer and Mach number effects on high-speed turbulent boundary layers. *J. Fluid Mech.* **974**, A10.

CROCCO, L. 1932 Sulla trasmissione del calore da una lamina piana a un fluido scorrente ad altavelocita. *L Aerotecnica* **12**, 181–197.

DEBIEVE, J.F., GOUIN, H. & GAVIGLIO, J. 1982 Momentum and temperature fluxes in a shock wave-turbulence interaction. *Struct.Turbul.Heat Mass Transfer*, 277–296.

VAN DRIEST, E.R. 1951 Turbulent boundary layer in compressible fluids. *J. Aeronaut. Sci.* **18** (3), 145–160.

DUAN, L., BEEKMAN, I. & MARTIN, M.P. 2011 Direct numerical simulation of hypersonic turbulent boundary layers. Part 3. Effect of Mach number. *J. Fluid Mech.* **672**, 245–267.

DUAN, L. & MARTIN, M.P. 2011 Direct numerical simulation of hypersonic turbulent boundary layers. Part 4. Effect of high enthalpy. *J. Fluid Mech.* **684**, 25–59.

FRISCH, U. & DONNELLY, R.J. 1996 *Turbulence: the Legacy of AN Kolmogorov*. AIP.

FU, L., KARP, M., BOSE, S.T., MOIN, P. & URZAY, J. 2021 Shock-induced heating and transition to turbulence in a hypersonic boundary layer. *J. Fluid Mech.* **909**, A8.

GAVIGLIO, J. 1987 Reynolds analogies and experimental study of heat transfer in the supersonic boundary layer. *Intl J. Heat Mass Transfer* **30** (5), 911–926.

GEROLYMOS, G.A. & VALLET, I. 2024 Total and static temperature statistics in compressible turbulent plane channel flow. *J. Fluid Mech.* **978**, A25.

GIBIS, T., SCIACOVELLI, L., KLOKER, M. & WENZEL, C. 2024 Heat transfer effects in compressible turbulent boundary layers a regime diagram. *J. Fluid Mech.* **995**, A14.

GRIFFIN, K.P., FU, L. & MOIN, P. 2021 Velocity transformation for compressible wall-bounded turbulent flows with and without heat transfer. *Proc. Natl. Acad. Sci. USA* **118** (34), e2111144118.

GUARINI, S.E., MOSER, R.D., SHARIFF, K. & WRAY, A. 2000 Direct numerical simulation of a supersonic turbulent boundary layer at Mach 2.5. *J. Fluid Mech.* **414**, 1–33.

GUPTA, V., MADHUSUDANAN, A., WAN, M., ILLINGWORTH, S.J. & JUNIPER, M.P. 2021 Linear-model-based estimation in wall turbulence: improved stochastic forcing and eddy viscosity terms. *J. Fluid Mech.* **925**, A18.

HUANG, J., DUAN, L. & CHOUDHARI, M.M. 2022 Direct numerical simulation of hypersonic turbulent boundary layers: effect of spatial evolution and Reynolds number. *J. Fluid Mech.* **937**, A3.

HUANG, P.G., COLEMAN, G.N. & BRADSHAW, P. 1995 Compressible turbulent channel flows: DNS results and modelling. *J. Fluid Mech.* **305**, 185–218.

HUTCHINS, N. & MARUSIC, I. 2007 Evidence of very long meandering features in the logarithmic region of turbulent boundary layers. *J. Fluid Mech.* **579**, 1–28.

MAEDER, T., ADAMS, N.A. & KLEISER, L. 2001 Direct simulation of turbulent supersonic boundary layers by an extended temporal approach. *J. Fluid Mech.* **429**, 187–216.

MARTIN, M.P. 2007 Direct numerical simulation of hypersonic turbulent boundary layers. Part 1. Initialization and comparison with experiments. *J. Fluid Mech.* **570**, 347–364.

MO, F., LI, Q., ZHANG, L. & GAO, Z. 2023 Direct numerical simulation of hypersonic wall-bounded turbulent flows: an improved inflow boundary condition and applications. *Phys. Fluids* **35**, 3.

MORKOVIN, M.V. 1962 Effects of compressibility on turbulent flows. *Mécanique De LA Turbulence* **367** (380), 26.

PIROZZOLI, S., GRASSO, F. & GATSKI, T.B. 2004 Direct numerical simulation and analysis of a spatially evolving supersonic turbulent boundary layer at M = 2.25. *Phys. Fluids* **16** (3), 530–545.

RUBESIN, M.W. 1990 Extra compressibility terms for Favre-averaged two-equation models of inhomogeneous turbulent flows. Tech. Rep. NASA.

SMITS, A.J., MCKEON, B.J. & MARUSIC, I. 2011 High–Reynolds number wall turbulence. *Annu. Rev. Fluid Mech.* **43**, 353–375.

SONG, Y., ZHANG, P. & XIA, Z. 2023 Predicting mean profiles in compressible turbulent channel and pipe flows. *Phys. Rev. Fluids* **8** (3), 034604.

SPALART, P.R., STRELETS, M. & TRAVIN, A. 2006 Direct numerical simulation of large-eddy-break-up devices in a boundary layer. *Intl J. Heat Fluid Flow* **27** (5), 902–910.

SUBBAREDDY, P. & CANDLER, G. 2012 DNS of transition to turbulence in a Mach 6 boundary layer. In *43rd AIAA Thermophysics Conference*, pp. 3106. AIAA.

TRETTEL, A. & LARSSON, J. 2016 Mean velocity scaling for compressible wall turbulence with heat transfer. *Phys. Fluids* **28** (2), 026102.

WALZ, A. 1962 Compressible turbulent boundary layers, 299–350.

WANG, L., HU, R. & ZHENG, X. 2021 A scaling improved inner–outer decomposition of near-wall turbulent motions. *Phys. Fluids* **33** (4), 045120.

XU, D., WANG, J. & CHEN, S. 2023 Reynolds number and wall cooling effects on correlations between the thermodynamic variables in hypersonic turbulent boundary layers. *J. Fluid Mech.* **965**, A4.

XU, S. & MARTIN, M.P. 2004 Assessment of inflow boundary conditions for compressible turbulent boundary layers. *Phys. Fluids* **16** (7), 2623–2639.

YING, A., LI, Z. & FU, L. 2024 The generalised resolvent-based turbulence estimation with arbitrarily sampled measurements in time. *J. Fluid Mech.* **998**, A3.

ZHANG, C., DUAN, L. & CHOUDHARI, M.M. 2018 Direct numerical simulation database for supersonic and hypersonic turbulent boundary layers. *AIAA J.* **56** (11), 4297–4311.

ZHANG, P.J.Y., WAN, Z.H., LIU, N.S., SUN, D.J. & LU, X.Y. 2022 Wall-cooling effects on pressure fluctuations in compressible turbulent boundary layers from subsonic to hypersonic regimes. *J. Fluid Mech.* **946**, A14.

ZHANG, Y.S., BI, W.T., HUSSAIN, F. & SHE, Z.S. 2014 A generalized Reynolds analogy for compressible wall-bounded turbulent flows. *J. Fluid Mech.* **739**, 392–420.